Pulsed laser engineering of composite submicron particles in colloidal systems: a high-performance catalyst for ethanol fuel cells

Mohammad Sadegh Shakeri, Oliwia Polit, Tatiana Itina, Jacek Gurgul, Joanna Depciuch, Magdalena Parlinska-Wojtan, Tomasz Roman Tarnawski, Andrzej Dziedzic, Olga Adamczyk, Naoto Koshizaki, et al.

▶ **To cite this version:**

Mohammad Sadegh Shakeri, Oliwia Polit, Tatiana Itina, Jacek Gurgul, Joanna Depciuch, et al.. Pulsed laser engineering of composite submicron particles in colloidal systems: a high-performance catalyst for ethanol fuel cells. Composites Part B: Engineering, In press, ⟨10.1016/j.compositesb.2025.112457⟩. ⟨hal-05012284⟩

HAL Id: hal-05012284

https://hal.science/hal-05012284v1

Submitted on 31 Mar 2025

HAL is a multi-disciplinary open access archive for the deposit and dissemination of scientific research documents, whether they are published or not. The documents may come from teaching and research institutions in France or abroad, or from public or private research centers.

L'archive ouverte pluridisciplinaire **HAL**, est destinée au dépôt et à la diffusion de documents scientifiques de niveau recherche, publiés ou non, émanant des établissements d'enseignement et de recherche français ou étrangers, des laboratoires publics ou privés.

HAL Authorization

Journal Pre-proof

Pulsed laser engineering of composite submicron particles in colloidal systems: a high-performance catalyst for ethanol fuel cells

Mohammad Sadegh Shakeri, Oliwia Polit, Tatiana Itina, Jacek Gurgul, Joanna Depciuch, Magdalena Parlinska-Wojtan, Tomasz Roman Tarnawski, Andrzej Dziedzic, Olga Adamczyk, Naoto Koshizaki, Shota Sakaki, Marcin Zając, Krzysztof Matlak, Zaneta Swiatkowska-Warkocka

PII: S1359-8368(25)00358-0

DOI: https://doi.org/10.1016/j.compositesb.2025.112457

Reference: JCOMB 112457

To appear in: *Composites Part B*

Received Date: 31 January 2025

Revised Date: 18 March 2025

Accepted Date: 26 March 2025

Please cite this article as: Shakeri MS, Polit O, Itina T, Gurgul J, Depciuch J, Parlinska-Wojtan M, Tarnawski TR, Dziedzic A, Adamczyk O, Koshizaki N, Sakaki S, Zając M, Matlak K, Swiatkowska-Warkocka Z, Pulsed laser engineering of composite submicron particles in colloidal systems: a high-performance catalyst for ethanol fuel cells, *Composites Part B*, https://doi.org/10.1016/j.compositesb.2025.112457.

This is a PDF file of an article that has undergone enhancements after acceptance, such as the addition of a cover page and metadata, and formatting for readability, but it is not yet the definitive version of record. This version will undergo additional copyediting, typesetting and review before it is published in its final form, but we are providing this version to give early visibility of the article. Please note that, during the production process, errors may be discovered which could affect the content, and all legal disclaimers that apply to the journal pertain.

© 2025 Published by Elsevier Ltd.

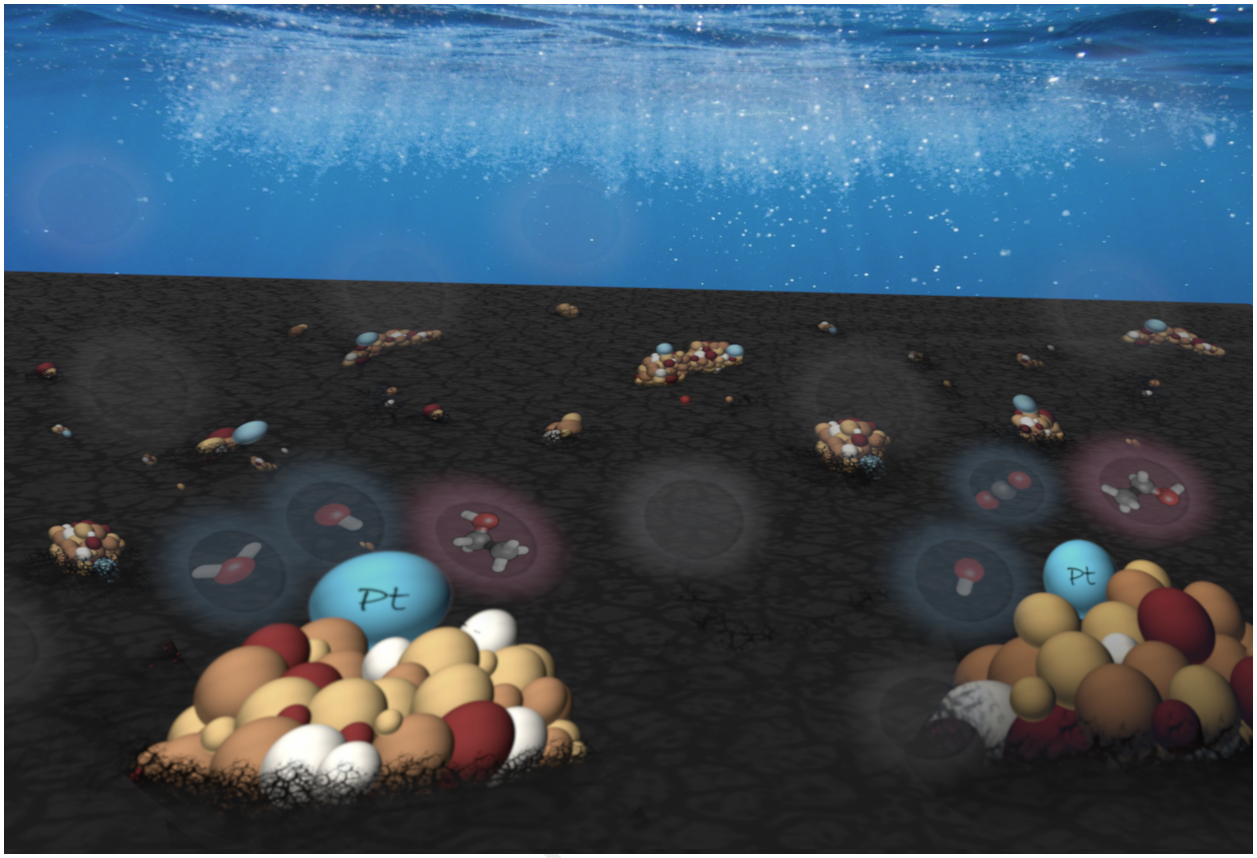

Journal

Journal Pre-proof

Pulsed laser engineering of composite submicron particles in colloidal systems: a high-performance catalyst for ethanol fuel cells

Mohammad Sadegh Shakeri[1,], Oliwia Polit[1], Tatiana Itina[2], Jacek Gurgul[3], Joanna Depciuch[1,4], Magdalena Parlinska-Wojtan[1], Tomasz Roman Tarnawski[1], Andrzej Dziedzic[5], Olga Adamczyk[1,6], Naoto Koshizaki[7], Shota Sakaki[7], Marcin Zając[8], Krzysztof Matlak[8], Zaneta Swiatkowska-Warkocka[1,*]*

1. Institute of Nuclear Physics Polish Academy of Sciences, PL-31342 Krakow, Poland
2. Université Jean Monnet Saint-Etienne, CNRS, Institut d Optique Graduate School, Laboratoire Hubert Curien UMR 5516, F-42023, SAINT-ETIENNE, France
3. Jerzy Haber Institute of Catalysis and Surface Chemistry, Polish Academy of Sciences, Niezapominajek 8, 30-239 Krakow, Poland
4. Department of Biochemistry and Molecular Biology, Medical University of Lublin, Lublin, 20-059 Poland
5. College of Natural Sciences, University of Rzeszow, Pigonia 1, 35-310 Rzeszow, Poland
6. Cracow University of Technology, Podchorążych 1, 30-084 Krakow, Poland
7. Graduate School of Engineering, Hokkaido University, Kita 13 Nishi 8, Kita-ku, Sapporo 060-8628, Japan
8. SOLARIS National Synchrotron Radiation Centre, Jagiellonian University, Krakow, 30-392 Poland

* Corresponding Author 1,
Mohammad Sadegh Shakeri (M.S. Shakeri)
Email: ms.shakeri@ifj.edu.pl
Phone No.: +48 515019092

*Corresponding Author 2,
Zaneta Swiatkowska-Warkocka (Z. Swiatkowska-Warkocka)
Email: zaneta.swiatkowska@ifj.edu.pl
Phone No.: +48 607138623

Journal Pre-proof

Journal Pre-proof

Abstract

Nanoparticles are widely regarded as optimal for catalytic reactions; however, larger particles with highly active surfaces may offer an intriguing alternative for advancing catalytic technologies. This study employs pulsed laser melting to transform colloidal copper/magnetite nanoparticles into surface-active submicron $Cu_xFe_{3-x}O_4$-Cu_yO-Cu_zFe_{1-z} composite particles, tailored for ethanol oxidation fuel cells. The findings reveal that colloidal particles tend to cluster into either homogeneous or heterogeneous aggregates, mediated by the surrounding liquid. This clustering aids the formation of desired phases during pulsed laser processing. Temperature-dependent thermodynamic phase transitions, combined with pulse-driven heating-cooling dynamics, promote copper oxidation and magnetite reduction, achieving both compositional control and microstructural surface activation. The synthesized heterostructures demonstrated excellent performance in ethanol oxidation, both as primary catalytic materials and as activity-enhancing supports for platinum. Oxidation state analysis post electrocatalysis indicated a reduction in graphite bonds and an increase in oxygen bonds, attributed to the high oxygen content of the catalysts' surface. The electrocatalysis ethanol oxidation process generated potent oxidizing agents, including ozone, oxygen and hydroxyl radicals, with the ability of degrading the sp^2 hybrid structure of graphite. Despite their submicron size, the kinetically activated composite particles exhibited exceptional surface activity, positioning them as cost-effective alternatives to the conventional catalysts for fuel cell technologies.

Keywords: Laser-colloid interaction; Submicron composite particles; Molecular dynamics; Oxidation-reduction phenomena; Electrocatalysis ethanol oxidation

Journal Pre-proof

Journal Pre-proof

1. Introduction

The interplay between lasers and matter has long captivated the scientific community, offering unparalleled opportunities for the precision synthesis of advanced materials [1-3]. Pulsed laser irradiation in suspension (PLIS) also known as pulsed laser melting in liquid (PLML) has emerged as a transformative approach in this field, enabling the production of composite particles with tailored compositions, architectures, and properties. This technique relies on the absorption of laser energy by nanoparticles suspended in a liquid medium, triggering rapid, localized heating that leads to melting and subsequent phase formation. Remarkably, solvent molecules, being largely transparent to the laser wavelength, remain thermally unaffected, preserving ambient conditions and enabling unique thermochemical reactions at the nanoparticle-solvent interface [4-10]. The rapid heating-cooling cycles intrinsic to PLIS drive phase transformations that frequently deviate from thermodynamic equilibrium, facilitating the formation of metastable or kinetically stabilized phases, especially on the surface of particles [4]. Phase formation during PLIS is governed by a complex interplay of nanoparticle temperature, solvent dissociation, and interfacial interactions [11-15]. When laser energy is absorbed, nanoparticles experience significant temperature increases, initiating bond dissociation in nearby solvent molecules. These dissociated species then diffuse into the molten nanoparticles, driving phase formation through bond reorganization. Factors such as laser fluence, nanoparticle size, solvent composition, and pulse dynamics play critical roles in shaping these transformations. Despite its immense potential, PLIS remains underexplored, particularly regarding the precise mechanisms governing phase transitions and the role of kinetics in stabilizing unique phases which could be beneficiary for catalytic reactions [16].

In this study, we harness PLIS to synthesize submicron Cu-Fe-O heterostructures, a material system recognized for its exceptional catalytic properties. Copper-based materials, including Cu oxides and ferrites, have garnered attention for their diverse applications in catalysis, clean energy generation, and sensor technologies [17-29]. Copper exhibits high catalytic activity, thermal conductivity, and chemical stability, making it a cornerstone material in electrocatalysis and photocatalysis. Similarly, ferrites such as $CuFe_2O_4$ are prized for their spinel structure, high magnetic stability, and excellent performance in energy-related applications, including Li-ion batteries and electrochemical cells [30-40]. Cu-Fe-O heterostructures, which integrate the catalytic properties of copper and the magnetic functionality of ferrites, hold significant promise for ethanol oxidation fuel cells. Their magnetic properties facilitate catalyst separation and reuse via external magnetic fields, enhancing recyclability. Additionally, spin-polarized electron transfer in ferrite phases may influence charge transfer dynamics, potentially improving catalytic efficiency [41-45]. Ethanol oxidation is a critical process in energy conversion technologies, with its efficiency heavily dependent on the catalyst's activity, durability, and resistance to deactivation. The lower toxicity and cost-effectiveness of ethanol make it a suitable and promising fuel for energy systems aimed at reducing dependence on fossil fuels. In a direct ethanol fuel cell (DEFC), ethanol is oxidized to carbon dioxide and water, consuming hydroxyl anions during the

process. Conventional DEFCs have typically relied on platinum and palladium as catalysts, due to their high efficiency in promoting ethanol oxidation. However, these precious metals suffer from limitations, including high cost, low abundance, and surface poisoning by carbon monoxide, leading to reduced catalytic performance over time [46-49].

In recent years, there has been a growing interest in developing low-cost and efficient electrocatalysts to replace platinum and palladium in DEFCs. One promising alternative is the use of copper-based materials, which exhibit excellent catalytic activity for ethanol oxidation, especially in metallic and oxide forms. Copper oxides, such as CuO and $CuFe_2O_4$, offer superior catalytic performance, with the ability to activate C-H bonds in ethanol molecules and facilitate the oxidation reaction. These materials exhibit a combination of active sites and varying oxidation states that are critical for enhancing reaction kinetics, improving resistance to deactivation, and achieving long-term stability. In particular, $CuFe_2O_4$ and similar mixed metal oxides and alloys are known to benefit from synergistic effects between copper and iron species, improving catalytic efficiency and enabling sustainable operation [50-52].

Beyond fundamental electrocatalytic studies, the scalability of the synthesis method is an essential factor for real-world applications. Pulsed laser irradiation of colloid as a novel synthesis method allows for continuous catalyst production in a liquid-phase environment. Compared to conventional laser ablation in liquids (LAL), which typically yields milligram-to-gram quantities per hour, our method demonstrates one to two orders of magnitude higher productivity. This suggests that the material yield can reach the gram-to-kilogram per hour range when scaled with higher-power laser sources and parallel beam configurations, making it a promising technique for industrial catalyst production [2, 4].

Our approach leverages the precise compositional control and phase-tuning capabilities of PLIS to synthesize heterostructures optimized for electrocatalysis ethanol oxidation reactions. By systematically varying key parameters, including laser fluence, solvent type, nanoparticle size, and Cu/Fe_3O_4 ratios, we aim to achieve fine control over the microstructure and composition of the synthesized particles. Detailed thermodynamic modeling and molecular dynamics simulations provide insights into phase stability and formation mechanisms, shedding light on the kinetics driving these transformations. Additionally, we analyze the oxidation state variations and microstructural characteristics of the synthesized submicron particles. The resulting heterostructures are tested both as primary catalysts and as supports for platinum catalysts, with oxidation state analysis before and after electrocatalysis revealing changes in surface chemistry. This investigation not only advances the understanding of laser-suspension interactions and phase formation mechanisms but also establishes a novel platform for developing next-generation catalytic materials. By bridging fundamental insights with practical applications, our work positions PLIS as a powerful tool for engineering heterostructures tailored to meet the demands of modern electrocatalysis and energy conversion technologies, particularly in the development of low-cost, high-performance catalysts for ethanol oxidation fuel cells.

2. Experimental and modeling procedure

2.1. Synthesis

In this study, raw nanoparticles including copper (obtained from US Research Nanomaterials with a purity of 99.9% and a size of 40 nm) and magnetite nanoparticles (two variants - one bought from US Research Nanomaterials with a purity of 99.5% and a size of 30 nm, and the other produced using conventional co-precipitation from $FeCl_2$ and $FeCl_3$ with an average size of 6 nm) were employed. Nanoparticles were dispersed in ethanol (POCH solvent, 99.8% purity) to create suspensions with a concentration of 0.0027 grams per liter. These suspensions were then treated with an ultrasonic device before being transferred into a sealed cell with a transparent quartz window (wavelength of 523 nm). An unfocused pulsed Nd:YAG laser operating at 523 nm with a frequency of either 10 or 33 Hz was utilized to irradiate the mixtures. Energy densities ranging from 200 to 300 mJ/cm^2 per pulse were applied to the colloidal suspensions for a duration of 60 minutes. The molar ratio of Copper (Cu) to Iron Oxide (Fe_3O_4) was consistently 1:1 in all samples, except for samples PLIS7 and PLIS8 where it was altered to 3:1 and 1:3, respectively. Ultrasonic agitation was implemented during the irradiation process to prevent sedimentation of suspended particles and agglomerates. The samples underwent coding based on variations in laser intensity, particle size, solvent type, powder molar ratio, and pulse repetition time (Table 1 and Fig. S1).

2.2. Characterizations

The structure of the particles obtained was analyzed using scanning electron microscope (SEM)-Hitachi S4800. To determine the average size of the particles, the diameters of 50 particles from each SEM image were measured. The crystal structure of the particles was examined using an X-ray diffractometer (XRD, PANalytical X'Pert Pro) with Cu K_α radiation ($\lambda = 1.54$ Å) at an operating current of 30 mA and voltage of 40 kV. The hydrodynamic diameter and Zeta potential of the particles were assessed using dynamic light scattering (DLS) with a Malvern Zetasizer Nano-ZS instrument equipped with a He-Ne laser (wavelength of 633 nm) at a backscattering angle of 173°. The nanoparticles microstructure were examined using scanning transmission electron microscopy (STEM) with the High Angle Annular Dark-Field detector (HAADF). This analysis was performed in both standard and high-resolution modes on a cutting-edge FEI Titan electron microscope operating at 300 kV. The microscope was equipped with aberration correction and a field emission gun (FEG) cathode to ensure accurate imaging. To determine the chemical composition of the nanoparticles, Energy Dispersive X-ray Spectroscopy (EDS) was utilized. The EDS analyses were conducted using a FEI Talos Transmission Electron Microscope (TEM) operating at 200 kilovolts, equipped with a Field Emission Gun (FEG) cathode and four in-column EDS detectors as part of the Super EDS system. Finally, a FEI Tecnai Qsiris, 200kV transmission electron microscope (TEM) was used to produce the high-resolution images for d-spacing analysis by fast Fourier transform (FFT). X-ray Photoelectron Spectroscopy (XPS) investigations were carried out in a multi-chamber Ultra-High Vacuum (UHV) setup with a SES R4000 hemispheric energy analyzer from Gammadata Scienta and a non-monochromatic AlKα source (12 kilovolts, 15

milliamperes). Additional information on the XPS measurements can be found in the corresponding authors' recent publication [16]. Since nanoparticles analyzed by XPS were placed on a silicon substrate, adjustments had to be made to account for the low conductivity of the system. Calibration was performed to set the binding energy (BE) of the alkyl (C-C/C-H) component of the C 1s spectrum at 285.0 electron volts. Finally, the optical properties of synthesized particles were characterized by UV-vis absorption spectroscopy (UV/VIS Helios Alpha by UNICAM) and fluorescence spectroscopy (Varian Eclipse).

2.3. Phase diagrams

2.3.1. Laser-based phase diagrams

The temperature of the particles was calculated according to the procedure described in [16]. The laser fluence required for each transition as a function of particle size (J-D diagram) and the maximum temperature of the particles (T-D diagram) were calculated as follows,

$$J\sigma_{abs}^{\lambda}(d) = m_p \Delta H \quad (1)$$

Here, J is the laser fluence (J.cm^{-2}pulse^{-1}), σ_{abs}^{λ} is the absorption cross-section of particles (cm^2), m_p is the particle mass (g), and ΔH is the enthalpy of the particles (J g^{-1}).

Mie theory was used to calculate the absorption efficiency of particles using MiePlot software (ver. 4620, http://www.philiplaven.com/mieplot.htm). To calculate the enthalpy of the phases, the reaction pathway was first determined by analyzing the Gibbs free energy of the probable transitions and reactions for each constituent phase. The reaction pathway and the calculation of the enthalpy of copper have been reported previously [49]. The enthalpy of Fe_3O_4 was calculated as,

$$\Delta H = \int_{T_0}^{T_m} C_P^{Fe_3O_4(s)}(T)dT + \Delta H_m + \int_{T_m}^{T_{Fe_3O_4(l)\rightarrow FeO(l)}} C_P^{Fe_3O_4(l)}(T)dT + \Delta H_{Fe_3O_4(l)\rightarrow FeO(l)} + \int_{T_{Fe_3O_4(l)\rightarrow FeO(l)}}^{T_{FeO(l)\rightarrow FeO(g)}} C_P^{FeO(l)}(T)dT + \Delta H_{FeO(l)\rightarrow FeO(g)} \quad (2)$$

Where, $C_p^{Fe_3O_4(s)}$, $C_p^{Fe_3O_4(l)}$, and $C_p^{FeO(l)}$ (J g^{-1}K^{-1}) are the heat capacities of solid Fe_3O_4, liquid Fe_3O_4 and molten FeO, respectively. Moreover, ΔH_m, $\Delta H_{Fe_3O_4(l)\rightarrow FeO(l)}$ and $\Delta H_{FeO(l)\rightarrow FeO(g)}$ (J g^{-1}) are the latent heat of Fe_3O_4 fusion and Fe_3O_4(l)-FeO(l) and FeO(l)-FeO(g) transitions occurring at T_m, $T_{Fe_3O_4(l)\rightarrow FeO(l)}$, and $T_{FeO(l)\rightarrow FeO(g)}$ (K) temperatures, respectively.

The temperature evolution of the particles during simultaneous energy absorption and heat release was represented by temperature-time diagrams (T-t), which were calculated with,

$$\frac{dE}{dt} = \frac{dE_{abs}}{dt} - \frac{dq}{dt} \quad (3)$$

Here E is the energy of the particle, E_{abs} is the absorbed energy, and q is the heat dissipation from the particle. The above differential equation was solved numerically with the 4th order Rung-Kutta derivative using Matlab software (Ver. R2022a, https://www.mathworks.com).

2.3.2. Phase stability diagrams

Thermodynamic equilibrium in the Cu-Fe-O-C-H system was studied using the HSC Chemistry package (ver. 10.x, https://www.hsc-chemistry.com/). In addition, HSC is used to accurately calculate the heat capacity, enthalpy, and Gibbs free energy of the phases at different temperatures to determine the reaction pathway of the heated Cu and Fe_3O_4 phases.

2.4. Synchrotron-based measurements

2.4.1. X-ray absorption spectroscopy (XAS)

Suspensions irradiated by pulsed laser were deposited on the SiC substrate and allowed to dry in the air for X-ray absorption spectroscopy (XAS) analysis. Samples of finely powdered CuO, Cu_2O, FeO, Fe_2O_3, and Fe_3O_4 (obtained from Merck Co.), along with Cu and Fe foil, were prepared as reference materials for determining the phase percentages using the linear combination fitting (LCF) technique. The hard X-ray absorption spectra were captured at the ASTRA beamline, while the soft X-ray absorption spectra were obtained at the PIRX beamline of the National Synchrotron Radiation Center in Krakow, Poland (SOLARIS). Prior to each XAS measurement, the spectrum of the Cu or Fe metal foil was carefully recorded for calibration purposes. Subsequently, the spectra were imported into the XAS data processing software "Athena" for normalization and data extraction [53].

The LCF method was assessed by mathematically matching the X-ray absorption fine structure (EXAFS) of the resulting heterostructure particles with the recorded spectra for Cu, Fe, CuO, Cu_2O, FeO, Fe_2O_3, and Fe_3O_4 as a reference. We also used Feff software to calculate the reference spectra for CuFe and $CuFe_2O_4$ phases. The calculation procedure is explained in section (2.5.2). This method exploits the additive property of absorption for each species, where the proportions of the reference spectra are combined to reconstruct the desired spectrum. Although originally designed for X-ray absorption near edge structure (XANES), XANES derivative, or EXAFS spectra, we utilized it across the entire range of XAS in this study. The total absorption coefficient is expressed as a summation of different chemical forms or species, denoted as $Sample = \sum f_i(STD_i)$. Here, "Sample" signifies the best fit to the energy range of the sample spectrum, while f_i represents the scaling factors applied to each corresponding standard spectrum (STD_i). The scaling factor obtained through LCF reveals the proportions of individual phases present in the sample under analysis. The LCF subroutine was developed using the Athena software for XAS data analysis. Our implementation of LCF involved fitting the normalized μ(E) spectrum of the heterostructure samples against the reference spectra spanning from 8900 to 9300 eV for Cu K-edge and 7000-7600 for Fe K-edge. The relative weights of the species can range from 0 to 1, and the absorption edge energies remain constant throughout the analysis.

2.4.2. Scanning Transmission X-ray Microscopy (STXM)

Scanning Transmission X-ray Microscopy (STXM) analysis was conducted at the DEMETER beamline within the SOLARIS synchrotron facility. STXM microscopy is a technique used to visualize samples at a microscopic level by analyzing the intensity of X-rays that pass through the sample as it is scanned. The end-station where our experiments took place offered imaging capabilities at room temperature and

operated at pressures as low as 10^{-6} mbar, but could also be pressurized with helium to reach ambient pressure. The STXM we utilized with a maximum resolution limited by the size of the light spot utilized to illuminate the sample, down to 30 nm.

2.4.3. Attenuated Total Reflectance Infrared (ATR-IR)

Measuring samples was conducted at the Synchrotron Infrared Source for Spectroscopy and Imaging (SISSI-Bio) beamline in Elettra Synchrotron Trieste, Italy. The analysis performed at SISSI-Bio provides Attenuated Total Reflectance (ATR) infrared Spectro microscopy data that reveals molecular level details, specifically identifying any chemical contamination on the sample surface. Photons in the Mid-infrared range with energies corresponding to organic and inorganic bonds were utilized. Spectra from individual samples were obtained using the VIS-IR microscope Hyperion 3000 (Bruker Optics, Billerica, MA, US) coupled with a VERTEX 70 V in-vacuum interferometer (Bruker Optics, Billerica, MA, US). The Synchrotron IR emission served as the source with a 100 µm MCT (Mercury-Cadmium-Telluride) detector, averaging 512 scans at 4 cm^{-1} spectral resolution in transmission mode. A 15X cassegrain objective-condenser pair was utilized, with the view-through apertures set at 10×10 µm to collect individual signals. Additionally, samples were imaged using a 64×64 bidimensional array detector (FPA, Focal Plane Array) through the same optics (15X, in transmission mode as well), resulting in a pixel size of 2.62 µm over an area of 167×167 µm. The data underwent correction and analysis using the QUASAR software (https://quasar.codes).

2.5. Atomistic modeling

2.5.1. Molecular Dynamics (MD) simulations

3-dimensional system with cubic simulation box is constructed with the periodic boundary condition in all directions containing Cu and Fe spheres. Embedded Atom Method (EAM) potentials were utilized for study the dynamics of Cu and Fe spheres in high temperature. The canonical ensemble (NVT) is used for all MD simulations in conjunction with the Nosé-Hoover thermostat with a damping constant of 100 fs. Prior to the MD simulations, energy minimization was performed using the conjugate gradient algorithm to optimize the initial geometric configuration. Then the systems were NVT-equilibrated at 298 K for 5 ps. After reaching equilibrium, MD simulations are performed for the system. In MD simulations, the use of high temperatures to accelerate reactions is a common strategy to overcome limited computing power [54-57]. By the way, here we tried to use the temperature ranges calculated by thermodynamics equations in section (2.3.1). More importantly, the present study is a comparative study of different cases, so the absolute temperature used is less important. A time step of 1 fs is used, which has been shown to be suitable for high temperature simulations with classical MD [54]. The dynamic trajectory and binding data are recorded every 100 frames (100 fs). The simulation results were visualized using Visual Molecular Dynamics (VMD) programs [58].

2.5.2. Ab-initio calculations

Quantum Espresso (QE) software was used for relaxation of the structure of Cu, Fe, and Cu-Fe compounds [100-102]. DFT calculations began with atomic modeling. Then the models were relaxed

by minimizing the energy of the system and the self-consistent field (SCF) captured the minimized energy of the system. The Perdew-Burke-Ernzerhof (PBE) of the generalized gradient approximation (GGA) was utilized as exchange and interaction potentials. The Van der Waals (vdW) correction is adopted to describe long-range vdW interactions and the dipole-dipole interaction is employed in the case of an asymmetric arrangement of species. The cut-off energy of the electronic wavefunction was 600 eV, and the k-space integration is performed according to the Monkhorst-Park scheme fitted to the reciprocal space size of the crystal structure of the models. The geometry optimization of the model is terminated when the force on each ion is not stronger than 0.05 eV. We have used the pseudopotentials Cu.rel-pbesol-dn-kjpaw_psl.0.2.UPF, O.rel-pbesol-n-kjpaw_psl.0.1.UPF, Fe.rel-pbesol-spn-kjpaw_psl.0.2.1.UPF from http://www.quantum-espresso.org.

Moreover, the jfeff10 software (https://times-software.github.io/feff10/) was used to calculate the EXAFS and XANES spectra of the relaxed models using QE including Cu, CuO, Cu_2O, Fe, FeO, Fe_2O_3, Fe_3O_4, CuFe, and $CuFe_2O_4$. Accordingly, the supper cells of the above phases were relaxed using QE and the final atomic positions were used in jfeff10 for XAS calculations. The settings for the simulations were configured as follows: the RPATH parameter was set to 5.0, COREHOLE was set to FSR, EXAFS to 20.0, LDOS to -30 20 0.1, SIG2 to 0.01, SCF to 5.0 0 100 0.2 1, and EXCHANGE to 0 -2 1 -1. These settings were applied to all simulations.

2.6. Electrocatalyst tests

2.6.1. PLIS as the main catalyst material; preparation and imaging

To prepare the PLIS/C catalysts, 20 mg of Vulcan XC-72R carbon powder was first immersed in a 0.7 M aqueous solution of HNO_3 for 30 minutes at room temperature. After this treatment, the carbon was thoroughly rinsed with distilled water until a neutral pH was achieved, then dried at 100°C for 10 hours. To deposit the PLIS heterostructures onto the carbon support, the washed PLIS was dispersed in solution, sonicated for 30 minutes, and then added dropwise onto the Vulcan XC-72R under vigorous stirring. To introduce surface functional groups, the carbon was oxidized through exposure to an HNO_3 and H_2O solution. Following this, the mixture was continuously stirred overnight with a magnetic stirrer to ensure homogeneity. The resulting black powder was washed with ethanol and distilled water to remove any residual reactants, and dried at 80°C overnight (approximately 10 hours). To assess the distribution of PLIS on the carbon support, Energy Dispersive Spectroscopy (EDS) mapping was conducted using Scanning Electron Microscopy (SEM). For these analyses, a TESCAN VEGA 3 SBH SEM, equipped with a tungsten cathode, was used. PLIS/C samples were mounted on SEM stub sample holders covered with a carbon adhesive patch, imaged under high-vacuum conditions at an accelerating voltage of 20 kV, and analyzed with an EDS detector.

2.6.2. PLIS as the Catalyst support

In order to study the function of newly created PLIS heterostructures as a support for platinum catalyst, we prepared the catalyst materials using the same procedure described in section (2.6.1). Three samples – Pt, PLIS, and PLIS-Pt particles – were prepared to examine how they perform in catalyzing ethanol

Journal Pre-proof

oxidation under both acidic and alkaline conditions. Additionally, we carried out electrochemical tests and analyzed the IRRAS spectra following the procedures detailed in sections (2.6.2) and (2.6.3).

2.6.3. Electrochemical measurements

Electrochemical measurements were conducted using a BIO-LOGIC SP-200 potentiostat in a standard three-electrode electrochemical cell configuration. Catalyst inks were prepared by ultrasonically dispersing 2 mg of catalyst powder in a mixture of 400 µL isopropyl alcohol, 100 µL ultrapure water, and 10 µL of 5 wt.% Nafion solution for 30 minutes to ensure uniformity. A 10 µL aliquot of the ink suspension was then deposited onto a polished glassy carbon electrode (GCE), forming the working electrode. Cyclic voltammetry (CV) measurements were performed in an ethanol-containing solution to evaluate the ethanol oxidation reaction (EOR) activity of the catalysts. A glass electrochemical cell equipped with a platinum (Pt) counter electrode and a silver/silver chloride (Ag/AgCl) reference electrode was employed. The electrolyte solution, comprising 0.1 M NaOH and 0.5 M C_2H_5OH, was deoxygenated by purging with argon gas for 30 minutes prior to measurements. To assess the durability of the catalysts, a chronoamperometry test was conducted in 0.1 M NaOH and 0.5 M C_2H_5OH under a constant potential of 0.5 V vs. Ag/AgCl (3M KCl). Furthermore, accelerated stability tests were performed by subjecting the catalysts to 1000 consecutive potential cycles between -1 and 1.5 V vs. Ag/AgCl (3M KCl) at a scan rate of 100 mV/s in a 0.1 M NaOH solution. All measurements were conducted at room temperature to ensure consistency across tests.

Moreover, for PLIS samples as a catalyst support, CV, EOR curves, as well as chronoamperometry and stability tests were performed additionally in 0.1M HClO4 solution with or without 0.5M ethanol depending on the test performed.

2.6.4. The Infrared Reflection Absorption Spectroscopy (IRRAS) measurements

A Nicolet iS50 FT-IR spectrometer equipped with an MCT (mercury cadmium telluride) detector cooled by liquid nitrogen, an ATR accessory with a ZnSe crystal, and an electrochemical cell was employed for in situ spectroelectrochemical ATR-FTIR measurements. The setup utilized the same three-electrode configuration as described in the electrochemical experiments. Spectra were acquired over the 1000–3000 cm^{-1} range, with a spectral resolution of 2 cm^{-1}, and each spectrum was computed from an average of 64 scans. Prior to experimentation, the spectrometer was purged with argon (Ar), which was maintained as the purge gas throughout the measurements to prevent interference from atmospheric CO_2 and H_2O. The selectivity of the catalysts for ethanol oxidation to carbonate and acetate species was assessed by presenting spectra in absorbance units, calculated as $A = -\log(R/R_o)$, where R and R_o represent the reflected IR intensities of the sample and the reference single-beam spectra, respectively. The reference spectrum was collected at a potential of 0.05 V in a 0.5 M ethanol and 0.1 M NaOH solution for alkaline environment and in a 0.5 M ethanol and 0.1 M $HClO_4$ solution for acidic environment.

Journal Pre-proof

3. Results and discussions

3.1. Phase formation

Upon exposure to pulsed laser energy, a mixture of colloidal copper and magnetite in ethanol (PLIS1) undergoes a transformation leading to the formation of a dense network of nanoparticles with irregular shapes, ranging from tens of nanometers to larger spherical particles in the range of 100 to 350 nm (Fig. 1a and Fig. 2a). As the size of raw magnetite increases (PLIS2), the network of small irregular particles disappears, giving way to the creation of regular spherical particles with average diameters ranging from 300 to 550 nm (Fig. 1c and Fig. 2b). Further increasing the irradiation energy (PLIS4 and PLIS5) results in a significant enlargement of the particles, with sizes reaching up to 800 nm (Fig. 1b,d). A similar trend is observed when nanoparticles are dispersed in ethyl acetate (PLIS3 and PLIS6), with the average particle size ranging from 400 to 750 nm at higher laser fluence (Fig. 1e,f and Fig.S2). The findings from the EDX analysis indicate a potential connection between the size and composition/distribution of composite particles (Fig S4), a relationship that warrants further investigation.

XRD results indicate that magnetite is reduced and copper is oxidized, resulting in the formation of $CuFe_2O_4$ (JCPDS card no. 00-025-0283), CuFe (JCPDS card no. 00-049-1399), CuO (JCPDS card no. 01-074-1021), and Cu_2O (JCPDS card no. 01-075-1531) phases along with the remaining ingredient particles, in which the composition is highly influenced by the synthetic parameters (Table S1). The overall structure of the irradiated samples consists of a blend of $Cu_xFe_{3-x}O_4$, Cu_yO, and Cu_zFe_{1-z} phases, with varying values of x and z ranging from 0 to 1. Additionally, the presence of y in the compounds can take on values of 1 and/or 2.

By altering the Cu:Fe molar ratio, the distribution of particle sizes with predominant average sizes of 100 and 400 nm remains constant. This phenomenon is likely due to the emergence of two separate agglomerates type consisting of copper and magnetite as the central particles. In compositions rich in copper (PLIS7), $CuFe_2O_4$ particles are embedded in the matrix of copper/CuFe alloy, while in compositions rich in iron (PLIS8), the matrix of magnetite contains larger Cu_2O and CuFe particles. The frequency of pulse repetition has the highest impact on the formation of phases in the heterostructure (Fig. S3). A lower frequency (PLIS9) leads to more copper ferrite formation (Fig. 2c), while a higher frequency (PLIS10) results in more CuFe alloy formation (Fig. 2d). Increasing the repetition rate alters the chemical structure due to cumulative heating and modified reaction kinetics. Pulse-to-pulse heat accumulation prolongs high-temperature conditions, influencing phase stability and promoting CuFe alloy formation over ferrite oxides. Reduced cooling time leads to global heating, enabling high-energy phase transformations. Higher repetition rates also enhance solvent decomposition, increasing reducing species that favor metallic Cu and CuFe alloys over oxidized phases. Weakened XRD peaks suggest increased structural disorder and partial amorphization of iron-rich phases. Additionally, carbon and oxide shells become more pronounced, stabilizing metallic phases in a more reductive environment.

The distinguishing peaks for the (111) plane of fcc Cu at $2\theta = 43.2^{\circ}$ are nearly identical to the peaks for the (200) plane of CuFe at $2\theta = 43.3^{\circ}$. This suggests the formation of nanoparticles from the Cu_zFe_{1-z} alloy, as the characteristic peaks of the alloy are somewhat broader than those of pure Cu nanoparticles. This broader peak indicates a lower crystallinity in the Cu_zFe_{1-z} alloy, which is typical in less ordered structures found in alloys. Additionally, the primary peaks of Cu have shifted slightly towards higher angles, indicating a reduction in lattice constant due to the replacement of Cu crystal lattice by Fe [23]. Higher laser fluence enhances oxidation, as confirmed by increased Cu_2O, CuO, and $CuFe_2O_4$ formation in XRD. However, ethanol/ethyl acetate solvents introduce partial reduction, converting Fe_3O_4 to FeO or Fe. At extreme fluence, rapid vaporization may deplete oxygen, promoting CuFe alloy formation. XRD of PLIS10 suggests a competition between oxidation and reduction, with alloying favored under transient oxygen starvation.

The Gibbs free energy values of the potential compounds were computed to identify the reaction pathway of the particles (Table S2 and Fig. S5a). The absorption efficiency of the particles was also calculated to be utilized for depiction of phase diagrams illustrating the relationship between laser fluence, particle size, and final temperature (Fig. S5b,c). It was observed that the maximum temperature reached by Fe_3O_4 particles increased by laser fluence, leading to the formation of FeO in a limited range of particle size distribution. Based on the analysis of the reaction pathway, it was observed that copper and magnetite do not undergo significant physical phase transitions during pulsed laser melting (Fig. 2e,f). Due to the oxidizing nature of the solvents, copper oxides are likely to be formed, along with iron-copper compounds resulting from the diffusion of atoms in the molten phase and oxidation/reduction phenomena in the solvent-particle interface. Here, the results of temperature calculation also confirm the potential relationship between particle size and composition of composite particles which was previously observed and reported in Fig. S4.

The temperature profile analysis shows that while laser irradiation melts copper particles completely across all sizes, a variety of sizes of Fe_3O_4 spherical particles remain solid and only a small portion of the particles exceed their melting point (Fig. S5d,f). FeO, Fe_3O_4, $CuFe_2O_4$, CuO, and Cu_2O are likely phases in the Fe-Cu-O system, depending on the near-ambient oxygen pressure and temperature range of the particles (Fig. S6). The absence of carbon in 3-component stability diagrams yielded absence of Cu_xFe_y alloys which may be formed through reduction of oxide phases. When copper and iron have low vapor pressure, each element's low pressure favors oxide phase formation of the other element. According to dynamic heating-cooling phenomena, nanoparticles absorb pulsed laser energy through electron-lattice coupling, where excited electrons transfer energy to the lattice within picoseconds, leading to localized melting. Temperature gradients arise from differences in optical absorption and thermal conductivity. Heating rates, estimated via thermodynamic absorption equations, depend on pulse energy and material absorption efficiency, dictating the extent of melting. Cooling rates are governed by thermal diffusion into the solvent and conductive heat dissipation, influencing phase formation. These heating-cooling dynamics drive oxidation-reduction reactions and atomic diffusion,

Journal Pre-proof

determining the formation of Cu_zFe_{1-z} alloys, $Cu_xFe_{3-x}O_4$ compounds, or CuO, Cu_2O, and Fe-based oxides.

Zeta potential measurements show that the nanoparticles in ethyl acetate are more stable than in ethanol (Table S4 and Fig. S7). The higher zeta potential of the particles in ethyl acetate may show the tendency of the Cu and Fe_3O_4 particles to form agglomerates together, while in ethanol they prefer to form their own agglomerates individually. The effect of agglomeration on phase formation during the pulsed laser melting of Cu and magnetite in liquid media may follow a four-stage mechanism, detailing the progression of phase development: (I) initial homostructure agglomeration, (II) formation of heterostructure aggregates, (III) diffusion of smaller particles into a larger core particle, and (IV) subsequent phase formation (Fig. 2g). The homo- versus heterostructure preference in agglomerates, as well as the characteristics of the core particle, are strongly influenced by solvent properties and zeta potential, which play a key role in determining the resulting phases. This mechanism suggests that solvent interactions and particle surface charge significantly guide phase formation through their impact on the stability and structure of agglomerates. Fig. 2g presents a hypothesis for copper ferrite and CuFe alloy formation based on laser-colloid interactions. Phase formation is influenced not only by oxidative/reductive conditions but also by nanoparticle aggregation. Heterogeneous agglomerates, where Cu is surrounded by Fe_3O_4 or vice versa, impact energy transfer, local melting, and diffusion during laser irradiation. The surrounding phase acts as a thermal and chemical buffer, altering reaction kinetics and phase stability, ultimately shaping the final composition of CuFe-based compounds.

Here we hypothesizes that three key factors influence phase formation including (I) process temperature which dictates the energy landscape for phase transitions, (II) heating and cooling rates which control the kinetics of phase stability, and (III) local chemical environment which determines by the dissociation of solvent molecules and influences the accessible transition states during phase formation. Unlike temperature and cooling rates, the chemical environment introduces a high level of complexity due to its indefinite and dynamic nature, particularly in high-temperature nanoparticle-solvent interactions. Using the results shown here and also according to previous corresponding authors' work [16], we categorize synthetic parameters (laser, pulse, solvent, and nanoparticle parameters) based on their impact on these three key factors. The process temperature and heating-cooling rate are primarily influenced by the laser and pulse parameters, respectively. On the other hand, the local chemical environment is mostly affected by the nanoparticle and solvent parameters. This structured approach aims to provide a comprehensive understanding of how synthetic parameters can be optimized to achieve efficient and controlled phase formation (Fig. 2h).

To gain deeper insights into phase formation, we performed molecular dynamics (MD) simulations focusing on the dynamic interactions between a single copper particle and surrounding smaller iron particles. In these simulations, the molten copper sphere absorbed adjacent iron particles, promoting iron atom diffusion and ultimately leading to the formation of Cu-Fe compounds (Fig. 2i,j and Fig. S8). The resulting spherical copper-iron compounds observed within larger particles (Fig. 2a) provide strong

Journal Pre-proof

evidence of phase formation, corroborating the process of smaller particles being incorporated into larger, molten particles. This absorption and alloying phenomenon observed in MD simulations was particularly notable when the smaller iron particles remained close to ambient temperature, while the larger copper particle was in a molten state. This scenario mirrors a real-world situation where particles might undergo "indirect melting" in the regions shielded from direct laser exposure. Under these conditions, bulk diffusion occurs, allowing groups of atoms or particles to migrate collectively rather than individually, which facilitates the formation of new phases (Video 1). Conversely, in regions exposed directly to laser pulses where temperatures are significantly higher for all particles, complete melting of particles results in increased atomic kinetic energy. This state, observed on the illuminated side of the particles (referred to as "direct melting"), allows atoms and particles to move with greater freedom, promoting individual diffusion rather than coordinated, bulk movement (Video 2). As a result, atomic dispersion occurs more uniformly, minimizing the likelihood of cluster formation (Fig. S9 and Fig. S10). These observations suggest that the alloying mechanism is influenced not only by thermal gradients but also by whether the melting is induced directly or indirectly by laser exposure. This dual effect of laser-stimulated melting, direct on the light-exposed side and indirect on the shaded side, appears to play a critical role in the dynamics of alloy formation within the Cu-Fe system.

3.2. Oxidation state analysis

The high-resolution XPS spectra of Cu 2p, Cu LMM, Fe 2p, O 1s, and C 1s for all samples (Fig. S11, Fig. S12 and Table S5) enabled detailed characterization of the nanoparticles' chemical states, particularly the oxidation states of copper and iron. Given the inherent complexity of transition metal 2p spectra, accurately interpreting the spectra and achieving reliable quantification of the chemical states required careful consideration of additional spectral features. These include shake-up satellites, multiplet splitting, and plasmon loss structures, which were accounted for during the curve-fitting process to enhance accuracy in the assignment of oxidation states.

For accurate numerical fitting of Cu 2p spectra, four distinct spin-orbit components were used, corresponding to the 2p 3/2 and 2p 1/2 photoelectron peaks, along with additional satellite peaks. These shake-up satellites appear at higher binding energies (BE) relative to the main peaks and are observed exclusively for Cu^{2+} (d^9 configuration), serving as specific markers for the quantity of Cu^{2+} in the sample [58, 59]. The primary spectral component (55-74%) originates from metallic Cu^o or Cu^+ species. However, XPS analysis of Cu 2p lines does not enable quantitative distinction between Cu^o and Cu^+ ions or between octahedral Cu^{2+} and Cu^+, as their binding energies are too similar to resolve clearly [60-62]. In such cases, the Cu LMM Auger lines offer additional insight, which will be discussed below.

The secondary spectral component (15-27%) corresponds to oxides containing Cu^{2+}, within PLIS3 and PLIS6 samples showing significant Cu^{2+} contributions from hydroxide (15% and 18%, respectively). In other samples, this contribution remains below 10%, suggesting an elevated hydroxide presence in samples irradiated in ethyl acetate. The component with the lowest binding energy (930.5-931.4 eV) is attributed to differential surface charging of Cu particles on a silicon substrate, a phenomenon resulting

from the contrasting conductivity between the particles and the dielectric substrate, which produces regions with inhomogeneous electrical conductivity. This effect has been similarly reported for metallic Ru on MgO and SiO_2, as well as Ru/Ce nanoparticles on mesocellular foam silica [63, 64]. Overall, the Cu 2p spectra of all samples show weak shake-up satellites, indicating that Cu^{2+} is not the predominant species.

Cu LMM Auger lines, excited by X-rays, offer quantitative insights into Cu^o and Cu^+ content since their chemical shift (~2 eV) is sufficiently large, unlike in Cu 2p lines. However, a limitation persists with the minimal shift between the Cu LMM peaks for metallic Cu and CuO, and between Cu_2O and $Cu(OH)_2$ [65]. Despite this limitation, the influence of $Cu(OH)_2$ is likely minimal due to its metastability and tendency to transition into the more stable CuO phase. Analysis of Cu LMM Auger spectra reveals distinct variations in copper species across samples, particularly PLIS2 and PLIS3, when compared to others (Table 2). Specifically, sample PLIS2 shows a significant predominance of Cu^o and Cu^{2+} over Cu^+, with PLIS3 exhibiting a similar but less pronounced trend. In contrast, Cu^+ emerges as the dominant phase in the remaining samples. Notably, besides the primary peaks for Cu^+ and Cu^o + Cu^{2+}, additional peaks appear from other Cu LMM transition states [66, 67], complicating the quantitative interpretation of results.

The O 1s spectra for Cu samples reveal several distinct components: (i) metal-oxide peaks (BE < 531.5 eV) related to oxygen in copper and iron oxides; (ii) peaks associated with hydroxyl groups (BE = 532.3-532.7 eV); (iii) adsorbed water (BE = 534.0-535.3 eV); and (iv) a weak signal at BE > 535.8 eV, likely corresponding to oxygen in organic contaminants [60, 68]. Notably, two broad spectral components with slightly increased FWHM were sufficient to represent the oxide phases present on the surface. However, the similar binding energies of iron and copper oxides mean their individual contributions within the O 1s spectrum cannot be distinctly resolved, allowing only approximate quantification. The first group of metal-oxide (Me(1)-O) peaks, with BE values between 529.4-530.4 eV, includes lattice oxides such as CuO and Cu_2O [58, 60], as well as Fe_2O_3 and Fe_3O_4 [69]. The second metal-oxide group (Me(2)-O), observed between 530.8-531.5 eV, includes defective oxides like CuO, Cu_2O, and $Cu(OH)_2$ [58, 60], along with FeOOH [69, 70].

In the Fe 2p spectra, two distinct doublets and their associated satellites were identified, corresponding to Fe^{2+} (binding energy ~710.2 eV) and Fe^{3+} (~711.7 eV) species (Table 2) [71, 72]. Notably, both spectral components exhibited a shift of approximately ~1 eV toward lower binding energies for samples PLIS2 and PLIS3. This shift likely reflects the formation of various surface oxide phases, which may influence surface charging and aligns with prior observations. Specifically, the surface composition appears to favor Fe_3O_4, characterized by a lower binding energy (710.6 eV), over Fe_2O_3 or FeOOH, which present slightly higher binding energies of 711.0 eV and 711.2 eV, respectively [70, 73]. The Fe^{2+}/Fe^{3+} ratio is relatively consistent across samples, typically within the range of 0.8 to 1.0, except for sample PLIS3, which shows a notably lower ratio at approximately 0.4. In the case of PLIS6, due to the minimal iron content and lack of resolution between Fe 2p 3/2 and Fe 2p 1/2 peaks, a reliable curve-

fitting analysis was not feasible. Finally, in addition to simple oxides or hydroxides, the potential formation of $CuFe_2O_4$ bimetallic ferrite, whose spectroscopic properties align well with the data, should also be considered [74].

Total fluorescence yield (TFY) synchrotron X-ray absorption analysis reveals prominent peaks that align well with the Gaussian fits from XPS (Fig. 3a-d). TFY data, with a penetration depth of several micrometers, provides insights into the overall bulk composition of the particles, displaying subtle yet meaningful differences compared to the surface-level data obtained from XPS. These differences include a marked reduction in hydroxide phases within the bulk material. Conversely, total electron yield (TEY) signals, which are more surface-sensitive, yield results closely aligned with XPS analysis (Fig. S13). A key distinction between TEY and TFY is the presence of hydrogen- and water-related bands in TEY spectra, which are absent in TFY results, reflecting TFY's reduced surface sensitivity.

Absorption spectra at Cu and Fe K-edges exhibit distinct features, comprising a pre-edge, an excrescence, and a prominent peak (Fig. S14, S15 and Table S6, S7). These spectra, showcase the varying oxidation states within PLIS samples (Fig. 3e,f). The pre-edge energy remains relatively consistent across all samples for both edges. However, the energy of the main peak at the Cu K-edge decreases with higher laser fluence, indicating an increase in copper oxidation. Conversely, the behavior of the main Fe K-edge peak shift is inconsistent with laser energy; it increases for samples dispersed in ethanol and decreases for those dispersed in ethyl acetate. This suggests a greater formation of copper-iron alloy with higher laser fluence in ethyl acetate, while an increase in laser fluence in ethanol solvent leads to an enhanced formation of copper ferrite.

By employing linear combination fitting (LCF) with different oxidation state measurement references, we were able to confirm that the primary oxidation states present in the samples are Cu/Cu^{+} and Fe^{2+}/Fe^{3+} (Fig. S16, 17 and Table S8, S9). Additionally, we utilized the ab initio Green function (GW) approximation method to calculate the extended EXAFS spectra of reference phases containing both copper and iron. The LCF analysis of the EXAFS spectra from the calculated models (Fig. S18, 19 and Table S10) further supports the formation and illustrates the variations of CuFe and $CuFe_2O_4$ phases in the PLIS samples.

3.3. Surface and interfaces analysis

Upon examination of the particles' surface and interfaces of various samples, it was discovered that the particles exhibited high levels of crystallization (Fig. S20). Smaller particles displayed a single crystalline structure, whereas larger particles tended to have a multi-crystalline structure (Fig. S21, S22). Additionally, high oxygen phases were detected on the most defective surfaces, consistent with previous studies by the authors [16]. Here we also observed the presence of quantum dot particles with a radius of less than 5 nm, which were dispersed in the solvent after the irradiation process (Fig. 4a and Fig. S25). These particles were found to be decorating the larger particles after they had dried. The quantum dots were formed as a result of local surface vaporization of atoms from the particles, as observed previously by the authors in reactive bond molecular dynamics simulations [16]. The analysis

of the d-spacing from various parts of the particles in different samples confirmed the formation of copper ferrite and copper-iron alloy (Fig. S26, 27). In some instances, a thin layer of amorphous material (less than 5 nm thick) was observed on the particles due to a lack of process control during cooling (Fig. 4b and Fig. S28). This amorphous layer is an unavoidable consequence that has the potential to impact the catalytic properties of the samples that will be explored in detail in Section (3.5). The majority of the interfaces between the particles were identified as smooth interfaces, indicating that the particles did not have strong chemical bonds, but rather formed van der Waals aggregates. While the surface of the single-crystal particles appeared smooth, the multi-crystalline particles were found to have high defect surfaces, resulting in unique structures such as twinning in certain cases (Fig. 4c). Additionally, the interfaces between phases inside the larger particles suggested the presence of normal multi-phase particles with minimal interfacial defects (Fig. 4d and Fig. S23, 24). The discovery of particles in multiple size ranges and a detailed examination of their microstructure suggest the potential utilization of the pulsed laser melting method in high-tech applications. This study reveals new insights into the applicability of this technology in advanced industries.

3.4. Surface contamination and Optical properties

Because of the potential reactivity of the defective high oxidation state surface of the particles, we have decided to study the probable existence of organic pollutants caused by laser treatment in organic solvent using ATIR spectra and IR imaging methods. The ATIR spectra display inorganic bands below 1100 cm^{-1}, indicating the existence of inorganic phases that were also identified through other analytical techniques (Fig. S29). During the analysis, significant bands at 1150 cm^{-1} were discovered, associated with the stretching pattern of the C-O bond typically found in primary alcohols (Fig. 5a,b and Fig. S30). In addition, faint bands at 2350 cm^{-1} were also detected, indicating the stretching mode of the O=C=O bond stemming from carbon dioxide present in the surroundings, suggesting air contamination (Fig. S31, 32). Although the intensity of these bands varied across different samples, they consistently appeared in all samples tested. Moreover, no specific organic bands beyond C-H and O-H groups were detected after the pulsed laser treatment, indicating that the contaminants observed are common impurities from the atmosphere inherent in the process of inorganic synthesis. We determined that while organic substances play a significant role in the high temperature PLIS synthesis process, there is no notable organic surface contamination that would hinder the usability of the synthesized materials for ethanol oxidation reactions.

The spectral absorption characteristics of samples fabricated in ethanol differ from those prepared in ethyl acetate, with the former showing its maximum in shorter wavelengths (Fig. 5c). Heterostructures prepared in ethanol possess a smaller energy bandgap, potentially stemming from an increased presence of defect states and/or a different distribution of oxidation states in the heterostructure. Conversely, samples processed in ethyl acetate exhibit a sharper absorption edge, indicating a larger bandgap. This could be attributed to a more homogeneous phase with varying stoichiometry resulting in fewer defect states. The UV-Vis absorption spectrum of samples synthesized in ethanol reveals a broad tail,

Journal Pre-proof

suggestive of a significant presence of defect states within the bandgap. This phenomenon may be a consequence of the synthesis method, leading to a greater number of vacancies or disorder specially in the surface of the material. The broad tail signifies the existence of multiple electronic states that can be excited, indicating a more disordered structure. In contrast, samples created in ethyl acetate display a sharper tail, signifying fewer defect states, enhanced crystallinity and fewer disorder-induced states.

Luminescence spectrophotometry is a valuable tool in the study of photo/electrocatalysis, not only allowing for an in-depth analysis of electronic structure, but also providing insights into surface defects, oxygen vacancies, and the generation/recombination of charge carriers. Efficient carrier separation is advantageous for catalytic applications, as it prevents or slows down carrier recombination, thereby enhancing the process efficiency which is viable in heterostructures. By analyzing PL spectra with different excitation energy we observe the presence of signals in 550-650 region related to Cu_2O and Fe_3O_4 phases and also a shorter signal in 400-500 region which could be attributed to the presence of $CuFe_2O_4$ phase and/or oxygen vacancies and surface defects (Fig. 5d,e). The synthesized materials here not only applicable as electrocatalyst for ethanol oxidation, but also have enough potential to be utilized in photocatalysis applications (Fig. S33a, S34). The relaxation lifetime in samples can reflect how sensitive they are to changes in their structure. This sensitivity is greatly affected by the specific raw materials and solvent used in their production. While the laser energy intensity can impact the lifetime of the samples, the effect is not as significant as the influence of the initial components (Fig. 5f). Specifically, samples prepared in ethanol exhibit a longer lifetime compared to those prepared in ethyl acetate (Fig. S35 and Table S11). This trend aligns with the findings from UV-Vis absorption spectra (Fig. 5c), which indicate a higher presence of surface defects characterized by band tailing in the former. Additionally, the electronic structure of the heterostructure enables the separation of charge carriers, resulting in an extension of their lifetime. However, the estimated lifetime remains consistent across different transitions (Fig. S33b for PLIS5 sample), providing support for the effective separation of charge carriers within the sample.

3.5. Electrocatalysis

3.5.1. PLIS as the main electrocatalyst material

The effectiveness of ethanol oxidation in terms of electrode material accessibility to the electrolyte was assessed by conducting electrochemically active surface area (ECSA) tests on various samples. The results indicated that most samples exhibited similar and suitable ECSA values, with the highest recorded for PLIS4 at 34.24 (cm^2/mg) and the lowest for PLIS6 at 8.81 (cm^2/mg). Surprisingly, it was found that PLIS4 exhibited the lowest effectiveness among the samples tested, displaying an onset potential of 0.82 V vs. Ag/AgCl (3M KCl) which was the highest compared to the other samples (Fig. S36 and Table S12). Despite this, the EOR test unexpectedly identified PLIS4 as possessing the most favorable catalytic properties, surpassing other samples despite its highest onset potential (Fig. 6a,b). This contradiction was attributed to compositional variations in the samples.

The most effective electrocatalysts were found to be those irradiated in ethanol at a higher laser fluence (PLIS4/C and PLIS5/C), leading to the formation of ferrite-based phases within heterostructure agglomerates, with a higher concentration of copper ferrite. Additionally, despite their size which is measured to be the largest among all, samples synthesized in ethanol with the highest laser fluence exhibited more defects, resulting in a more active surface for catalytic reactions [75-77]. Therefore, the chemical composition and the presence of defects on the active surface were identified as key factors impacting the electrocatalytic behavior of ethanol oxidation in this study. The durability of PLIS4/C and PLIS5/C displaying the most effective catalytic behavior was initially investigated with chronoamperometry and then with accelerated stability testing. The current-time curves revealed an initial drop in current for both catalysts, followed by a gradual decay (Fig. 6c). Notably, the drop in current was delayed longer for the PLIS4/C sample, which boasted a current value approximately 15 times higher than the PLIS5/C catalyst. Additionally, after 1000 cycles, the durability of the analyzed catalysts showed a 20% increase in ECSA for the PLIS4/C catalyst (Fig. 6d). Moreover, by increasing the potential, we observed a decrease in HCO^{3-} /CO_3^{2-} signals and an increase in CH_3COO^- signals in the IRRAS spectra, with a more pronounced change in the PLIS4/C sample (Fig. 6e,f). This change was accompanied by a higher intensity of CO_2 signal, indicating a more complete oxidation of ethanol in the PLIS4/C catalyst, making it the most efficient catalyst.

The superior EOR performance of PLIS4 stems from enhanced copper ferrite formation, increased surface defects, and synergistic Cu-Fe oxide interactions. High laser fluence in ethanol promoted ferrite-based phases, known for their redox activity and surface oxygen enrichment. Absorption and photoluminescence analyses also confirm defect-rich surfaces, serving as active catalytic sites in PLIS4 sample. Furthermore, phase and elemental analysis reveal that the outer layer consists of Cu oxides (CuO, Cu_2O) and $CuFe_2O_4$, or Fe-containing species near Cu-rich regions, forming a heterogeneous interface. The presence of Cu oxides enhances EOR activity due to their redox properties, while $CuFe_2O_4$ provides additional oxygen adsorption sites. The heterostructure interface between Cu, Fe oxides, and ferrite phases improves charge transfer, boosting electrocatalytic performance.

3.5.2. Oxidation state variation during electrocatalysis

Synthesized materials created with PLIS exhibit an active surface, showcasing noticeable oxidation state alterations following both carbon compositing and electrocatalysis. An EDX elemental map verifies the consistent dispersion of copper and iron, key constituents of PLIS samples, on carbon prior to electrocatalysis. (Fig. S37). An in-depth examination of a spherical particle cluster located within the carbon bed in PLIS4/C catalyst after electrocatalysis demonstrates a heterostructure resembling CuFe and/or copper ferrite formed in the matrix of magnetite (Fig. 7a). The synchrotron-based STXM image and its associated spectra from various points on the particle confirm the presence of high-concentrated oxygen shell on the surface of particles. Upon conducting electrocatalysis measurements, a thorough analysis of this specific cluster revealed the presence of a highly concentrated oxygen-containing shell on the surface of the particles. This observation can be attributed to the creation of active environments

resulting from pulsed laser irradiation on the surface. Additionally, it serves as a clear indication of the formation of hydroxide phases, particularly on copper particles (Fig. S38).

The pulsed laser melting method in liquid allows for the modulation of the oxidation state of transition metals, leading to the creation of an active surface that can enhance catalytic reactivity when the synthetic parameters are properly adjusted. After electrocatalysis of PLIS/C catalysts, it was found that copper underwent oxidation and iron underwent reduction. Analysis of the oxidation states using synchrotron X-ray absorption showed an increase in the relative intensity of Cu^{2+}/Cu^{+} and Fe^{2+}/Fe^{3+} signals, confirming the mentioned oxidation state variations (Fig. 7b-e and Fig. S39). The key to enhancing the activity of catalyst material lies in fine-tuning the synthetic parameters in the pulsed laser melting method to produce low oxidation state copper and high oxidation state iron in the PLIS samples. To further investigate the oxidation state variations specially on the catalyst's surface, in-depth quantitative XPS analysis was conducted (Table 3). The C 1s XPS spectra of PLIS4/C before and after electrocatalysis have similar fitting peaks attributed to graphite (sp^2C hybridization, C–C bonds), amorphous carbon on the sample surface (sp^3C hybridization, C–H bonds) and carbides (C=C bonds) [82]. Moreover, three oxygen signals indicating oxide contamination are well seen: (i) carbon making a single bond with oxygen (C–O), (ii) carbon making a double bond with oxygen as in carboxyles or esters (O=C–O) or two single bonds with oxygen (O–C–O), and (iii) carbonate groups (O–(C=O)–O) [83]. The last tiny component was identified as $\pi \rightarrow \pi^{*}$ satellite. The sample after the reaction is characterized by fewer graphite bonds with an increase in oxygen bonds. The electrocatalysis reaction appeared to have produced strong oxidants, such as ozone, atomic oxygen radicals or hydroxyl radicals, which destroyed the sp^2 hybrid structure of graphite and generated C–OH, C–O–C, C=O and O=C–O groups (Fig. 7f). The oxygen peak was decomposed into three components. The first one at ~531.4 eV was attributed to inorganic oxygen in metal oxides (mainly Cu oxides) and to carbonyl oxygen making a double bond with carbon (including ketone C=O and ester O=C-O groups) [84]. It can be said that carbonyl oxygen is the most effective electron-withdrawing group because it has the lowest binding energy of the O 1s line. Metal hydroxides and oxygen making single bonds with carbon (C–O–H of hydroxyl and C–O–C of ether groups) are the second contribution that dominates the spectrum. The last component, at BE of 534.5 eV, can be attributed to oxygen in physiosorbed water and C–O bonds with aromatic carbon. Subjecting the sample to the process of electrocatalysis results in a significant increase in the number of hydroxyl groups on the surface at the expense of the other functional groups [85]. At the same time, the shift of the center of gravity of the Cu 2p spectrum toward higher binding energies shows that the electrocatalysis process is accompanied by an increase in the proportion of copper on the +2 oxidation state, and in particular on the formation of copper hydroxide. Due to the extremely small amount of iron on the surface of the samples, its quantitative analysis was not possible. Qualitatively, the spectra of both samples are similar, with a noticeably weaker signal-to-noise ratio in the sample after electrocatalysis with the similar measurement time, indicating a reduction in the amount of iron on the surface. These results confirm the predominant role of copper compounds in

driving electrocatalysis reactions within the heterostructure, with iron compounds playing a more supportive role. The shift of the Cu 2p XPS spectrum toward higher binding energies after the long-term stability test of the ethanol oxidation reaction (EOR) suggests an increase in the oxidation state of copper species on the catalyst's surface. This observation indicates that the electrocatalysis process is accompanied by an increase in the proportion of copper in the +2 oxidation state, particularly the formation of copper hydroxide. Such changes in oxidation state can significantly influence the catalytic properties of the material, as different oxidation states of copper exhibit varying catalytic activities.

3.5.3. PLIS as the support for Pt

The synthesized PLIS samples and platinum demonstrated their optimal catalytic activities in alkaline and acidic environments, respectively. Knowing this fact, we tried to evaluate the performance of the PLIS4 catalyst in both acidic and alkaline environments when it used as a platinum support in ethanol oxidation reaction (EOR) fuel cells.

3.5.3.1. Acidic environment

The electrochemical properties of Pt/C, PLIS/C, and PLIS-Pt/C catalysts were examined by CV to assess their efficacy in promoting EOR. Measurements in a 0.1 M $HClO_4$ solution using Ag/AgCl (3M KCl) as the reference electrode provided the ECSA for each catalyst (Fig. 8a). The ECSA values for Pt/C and PLIS-Pt/C catalysts were similar, suggesting comparable EOR performance, with all potentials referenced to Ag/AgCl (3M KCl) (Fig. S40 and Table S13). However, the current density during EOR was significantly different between Pt/C and PLIS-Pt/C, with PLIS-Pt/C exhibiting nearly double the current of Pt/C (Fig. 8b). Previous studies have highlighted the significance of physical interactions between metal and metal oxide particles in enhancing overall catalytic activity and durability for the ethanol oxidation reaction [86, 87]. In the case of copper oxide catalysts, electrocatalysis at negative potentials can lead to the transformation of metal oxides into their metallic form. Consequently, it is postulated that voltammetry-induced restructuring of the catalyst surface could offer a potential avenue for modulating the catalytic activity. A study conducted by Sun et al. revealed the significant impact of voltamperometric cycles on the dissolution of metal nanoparticles. The reduction of metal ions leads to changes in the morphology of copper catalysts, resulting in the formation of well-defined nanocrystalline copper catalysts [88]. Another study found that performing electro-oxidation reactions at high potentials can cause severe corrosion of cathode catalysts such as polycrystalline copper surfaces, and single crystalline platinum and copper [89]. Furthermore, for PLIS/C catalysts, both the ECSA and the current values in the EOR curve were observed to be very small (Fig. 8a,b). This aligns with existing literature suggesting that the catalytic activity of copper are optimized in an alkaline environment [90].

It was observed in the chronoamperometry test that as time progressed, the current values of all catalysts increased. The PLIS/C catalyst showed the highest increase, while the PLIS-Pt/C catalyst showed the smallest increase (Fig. 8c). Due to the superior catalytic properties of the PLIS-Pt/C catalyst, an accelerated stability test was conducted on this particular sample (Fig. 8d). The results of the accelerated

Journal Pre-proof

stability test indicated that the ECSA value of the analyzed catalysts increased after 1000 cycles, rising from 0.23 to 0.43 cm^2. This observation highlighted the potential of PLIS-Pt catalyst as a promising candidate for catalytic ethanol oxidation reaction in acidic media due to the metal-metal oxide transitions [91].

3.5.3.2. Alkaline environment

In the alkaline environment, all catalysts had comparably similar ECSA values (Fig. 9a). However, the EOR curves indicated that the PLIS/C catalyst had the highest current, while the Pt/C catalyst had the lowest (approximately three times less than PLIS/C). Additionally, the PLIS-Pt/C catalyst had a current value around 0.005 less than PLIS/C, suggesting that PLIS-Pt mixture exhibited catalytic properties in the alkaline environment (Fig. 9b). These findings were further supported by the onset potential values (Fig. S40 and Table S13) with the smallest value of 0.25V for PLIS-Pt/C and the highest value of 0.375 V for Pt/C.

Similar to the acidic conditions, the chronoamperometry test revealed that the current values increased over time for all the catalysts analyzed. The rate of increase was consistent across all catalysts. However, the greatest increase was observed in the Pt/C catalyst, while the smallest increase was seen in the PLIS/C catalyst (Fig. 9c). An accelerated stability test was conducted on the PLIS/C catalyst system and accordingly the electrochemically active surface area was measured before and after 1000 cycles (Fig. 9d). Prior to the cycles, the surface area was 2.575 cm^{-2}, and after the cycles, it decreased to 1.716 cm^{-2}, indicating a 34% decrease. Despite this decrease, the results still demonstrated that PLIS nanoparticles can effectively function as a catalyst in an alkaline environment.

3.5.3.3. In-situ measurement of catalytic reaction pathway

To determine the preferred catalytic pathway for carbonate or acetate production, we analyzed bands associated with CO_2, CO, CH_3CHO, and CH_3COOH, observed at 2347 cm^{-1}, 2118 cm^{-1}, 1550 cm^{-1}, and 1415 cm^{-1}, respectively. IRRAS spectra were obtained in various potentials monitoring changes in CO_2, CO, CH_3CHO, and CH_3COOH concentrations for PLIS/C and PLIS-Pt/C catalysts in both acidic and alkaline environments. For PLIS/C in acidic media (Fig. 7e, f), CO_2 signals were consistently weaker than CH_3CHO and CH_3COOH at all potentials, whereas PLIS-Pt/C displayed increased CO_2 signals with potential, indicating a shift towards complete oxidation (Fig. 7g, h). Under alkaline conditions, both PLIS/C and PLIS-Pt/C catalysts followed a similar trend, with CO_2 formation increasing at higher potentials (Fig. 8e-h). These results affirm the robust EOR potential of PLIS-Pt/C in both acidic and alkaline environments and PLIS/C in alkaline media (Fig. S41). *In-situ* measurements showed that the concentrations of CO_2, CO, CH_3CHO, and CH_3COOH increased over time, with CH_3CHO and CO_2 exhibiting the most significant growth. Ethanol oxidation primarily led to CH_3CHO and CH_3COOH via partial oxidation, while the higher CO_2 production indicated complete oxidation. These findings suggest that PLIS-Pt/C in acidic media and PLIS/C in alkaline media achieve optimal EOR performance, favoring the complete oxidation of ethanol to CO_2.

Finally, we evaluated synthesis reproducibility and catalyst stability by testing three independent PLIS4 batches and reanalyzing the original PLIS4 sample after 18 months (Fig. S42). The new batches exhibited comparable or higher electrocatalytic activity, confirming good reproducibility. Specifically, PLIS4.1 showed a 35% increase in activity, PLIS4.2 exhibited an 18% decrease, and PLIS4.3 demonstrated a 1.5-fold enhancement compared to the original PLIS4 sample. However, the aged PLIS4 sample showed a ~70% decline in activity, indicating potential long-term stability concerns. Future studies may focus on aging effects and degradation mechanisms for commercializing purposes.

4. Conclusions

The pulsed laser compositional tuning of colloidal copper/magnetite nanoparticles demonstrates the effective formation of submicron composite particles possessing promising catalytic properties due to highly active surface containing multiple oxidation states of transition metals. Here, we effectively studied the synthesis parameters, such as particle size, solvent, laser fluence, repetition rate, and Cu:Fe molar ratio, to show how they affect compositional tuning of the desired heterostructures. These parameters critically influenced the compositional and microstructural variations, affecting the formation of $Cu_xFe_{3-x}O_4$-Cu_yO-Cu_zFe_{1-z} heterostructure. We also categorized these synthetic parameters according to their prominent role on changing the key factors of phase formation i.e. process temperature, heating-cooling rate and local chemical environment. The research highlighted the mechanism of transformation process during pulsed laser-induced heating including melting of agglomerates, promoting unique phase formations and alloying between copper and magnetite particles. The oxidation states analyses further confirmed the presence of multiple oxidation states in both copper and iron surface, indicating complex redox interactions progressing copper oxidation and magnetite reduction during synthesis. Pulse-driven oxidation-reduction dynamics at the nanoparticle-solvent interface induce variability in x, y, and z within $Cu_xFe_{3-x}O_4$-Cu_yO-Cu_zFe_{1-z}. XRD, XAS, MD simulations, and laser-induced temperature modeling confirm the formation of $CuFe_2O_4$, CuFe, CuO, and Cu_2O phases, with XRD verifying Cu_yO (y = 1, 2). Peak broadening in fcc Cu (111) and CuFe (200) indicates alloy formation, while peak shifts suggest Fe incorporation into Cu, reducing its lattice constant. MD simulations reveal molten Cu absorbing Fe nanoparticles, forming Cu_zFe_{1-z} alloys. $Cu_xFe_{3-x}O_4$ formation results from Fe_3O_4 partial reduction during Cu incorporation into the spinel lattice, as supported by thermodynamic modeling and XAS. These findings highlight pulsed laser irradiation as a route to tunable phase transformations in composite synthesis. The structural and compositional versatility of the resulting composite particles facilitated high catalytic activity in ethanol oxidation, outperforming both individual oxides and previous composite catalysts. Specifically, the heterostructures served efficiently as both primary catalysts and as supports for platinum, significantly enhancing the electrochemical response. Moreover, oxidation state changes post-catalysis, particularly the increase in Cu^{2+}, suggested that the catalytic process fostered strong oxidizing agents, such as atomic

oxygen and hydroxyl radicals, which modified the surface composition and structure. Overall, this research showcases the potential of pulsed laser synthesis in tuning nanoparticle compositions for advanced catalytic applications, providing a controllable, scalable, and environmentally friendly approach to catalyst design. The study's outcomes underscore the synergistic effects within Cu-Fe-O systems, paving the way for further exploration of heterostructures in sustainable energy applications, especially for fuel cells and other catalytic processes.

Journal Pre-proof

Journal Pre-proof

Acknowledgments

This work was supported by the Polish National Science Centre, Programs No. 2022/06/X/ST3/01743 and 2018/31/B/ST8/03043. Part of the computational work was conducted in collaboration with the Prometheus Cluster at Cyfronet, AGH University of Science and Technology, Krakow, utilizing Grant No. PLG/2022/015573. This publication was also partially developed under the provision of the Polish Ministry and Higher Education project "Support for research and development with the use of research infra-structure of the National Synchrotron Radiation Centre SOLARIS" under contract nr 1/SOL/2021/2. The X-ray absorption spectroscopy measurements were performed at the SOLARIS synchrotron center in Krakow, Poland. Hard X-ray measurements were carried out at the ASTRA beamline by proposal number 232128, while soft X-ray measurements were conducted at the PIRX beamline by proposal number 239056. Synchrotron IR measurements were also completed at the Synchrotron Infrared Source for Spectroscopy and Imaging (SISSI-Bio) beamline in Elettra Synchrotron Trieste, Italy, under proposal no. 20237198, with additional support from the Central European Research Infrastructure Consortium (CERIC-ERIC). Scanning Transmission X-ray Microscopy (STXM) measurements were performed at the SOLARIS synchrotron center using proposal no. 232097. We would like to express our appreciation to the Department of Technical Chemistry I and the NETZ group at the University of Duisburg-Essen for their valuable assistance with our research on Photoluminescent and decay studies. We also extend our gratitude to the Department of Chemistry, University of Warsaw, for access to the Talos F200 FEI TEM instrument, co-financed by European Regional Development Fund under the Operational Program Innovative Economy, 2007–2013.

Journal Pre-proof

Ethical statement

The manuscript does not contain clinical studies or patient data.

Journal Pre-proof

Conflict of interests

The authors declare that they have no conflict of interest.

Journal Pre-proof

Journal Pre-proof

References

[1] Haibo Zeng, Xi-Wen Du, Subhash C. Singh, Sergei A. Kulinich, Shikuan Yang, Jianping He, and Weiping Cai. "Nanomaterials via laser ablation/irradiation in liquid: a review." *Advanced Functional Materials* 22, no. 7 (2012): 1333-1353.

[2] Jayaraman Theerthagiri, K. Karuppasamy, Ahreum Min, Durai Govindarajan, M. L. Kumari, Govarthanan Muthusamy, Soorathep Kheawhom, Hyun-Seok Kim, and Myong Yong Choi. "Unraveling the fundamentals of pulsed laser-assisted synthesis of nanomaterials in liquids: Applications in energy and the environment." *Applied Physics Reviews* 9, no. 4 (2022).

[3] Zhang, Dongshi, Zhuguo Li, and Koji Sugioka. "Laser ablation in liquids for nanomaterial synthesis: diversities of targets and liquids." *Journal of Physics: Photonics* 3, no. 4 (2021): 042002.

[4] Yoshie Ishikawa, Takeshi Tsuji, Shota Sakaki, and Naoto Koshizaki. "Pulsed laser melting in liquid for crystalline spherical submicrometer particle fabrication-Mechanism, process control, and applications." *Progress in Materials Science* 131 (2023): 101004.

[5] Vincenzo Amendola, David Amans, Yoshie Ishikawa, Naoto Koshizaki, Salvatore Scirè, Giuseppe Compagnini, Sven Reichenberger, and Stephan Barcikowski. "Room-temperature laser synthesis in liquid of oxide, metal-oxide core-shells, and doped oxide nanoparticles." *Chemistry–A European Journal* 26, no. 42 (2020): 9206-9242.

[6] Yoshie Ishikawa, Naoto Koshizaki, Alexander Pyatenko, Noriyuki Saitoh, Noriko Yoshizawa, and Yoshiki Shimizu. "Nano-and submicrometer-sized spherical particle fabrication using a submicroscopic droplet formed using selective laser heating." *The Journal of Physical Chemistry C* 120, no. 4 (2016): 2439-2446.

[7] Yoshie Ishikawa, Naoto Koshizaki, and Shota Sakaki. "Spherical particle formation mechanism in pulsed laser melting in liquid under controlled-pulse-number irradiation using a slit nozzle flow system." *The Journal of Physical Chemistry C* 123, no. 40 (2019): 24934-24942.

[8] Alexander Pyatenko, Hongqiang Wang, and Naoto Koshizaki. "Growth mechanism of monodisperse spherical particles under nanosecond pulsed laser irradiation." *The Journal of Physical Chemistry C* 118, no. 8 (2014): 4495-4500.

[9] Yoshie Ishikawa, Yoshiki Shimizu, Takeshi Sasaki, and Naoto Koshizaki. "Boron carbide spherical particles encapsulated in graphite prepared by pulsed laser irradiation of boron in liquid medium." *Applied Physics Letters* 91, no. 16 (2007).

[10] Hongqiang Wang, Naoto Koshizaki, Liang Li, Lichao Jia, Kenji Kawaguchi, Xiangyou Li, Alexander Pyatenko, Zaneta Swiatkowska-Warkocka, Yoshio Bando, and Dmitri Golberg. "Size-tailored ZnO submicrometer spheres: bottom-up construction, size-related optical extinction, and selective aniline trapping." *Advanced Materials* 23, no. 16 (2011): 1865.

[11] Hongqiang Wang, Kenji Kawaguchi, Alexander Pyatenko, Xiangyou Li, Zaneta Swiatkowska-Warkocka, Yukiko Katou, and Naoto Koshizaki. "General bottom-up construction of spherical particles

by pulsed laser irradiation of colloidal nanoparticles: a case study on CuO." *Chemistry–A European Journal* 18, no. 1 (2012): 163-169.

[12] M. S. Shakeri, O. Polit, B. Grabowska-Polanowska, A. Pyatenko, K. Suchanek, Mateusz Dulski, J. Gurgul, and Z. Swiatkowska-Warkocka. "Solvent-particles interactions during composite particles formation by pulsed laser melting of α-Fe_2O_3." *Scientific Reports* 12, no. 1 (2022): 11950.

[13] O. Polit, M. S. Shakeri, and Z. Swiatkowska-Warkocka. "Controlling the Magnetic Properties of Fe-Based Composite Nanoparticles." *Acta Physica Polonica: A* 145, no. 2 (2024).

[14] Hongqiang Wang, Masahiro Miyauchi, Yoshie Ishikawa, Alexander Pyatenko, Naoto Koshizaki, Yue Li, Liang Li, Xiangyou Li, Yoshio Bando, and Dmitri Golberg. "Single-crystalline rutile TiO_2 hollow spheres: room-temperature synthesis, tailored visible-light-extinction, and effective scattering layer for quantum dot-sensitized solar cells." *Journal of the American Chemical Society* 133, no. 47 (2011): 19102-19109.

[15] Shota Sakaki, Hiroshi Ikenoue, Takeshi Tsuji, Yoshie Ishikawa, and Naoto Koshizaki. "Pulse-width dependence of the cooling effect on sub-micrometer ZnO spherical particle formation by pulsed-laser melting in a liquid." *ChemPhysChem* 18, no. 9 (2017): 1101-1107.

[16] Mohammad Sadegh Shakeri, Zaneta Swiatkowska-Warkocka, Oliwia Polit, Tatiana Itina, Alexey Maximenko, Joanna Depciuch, Jacek Gurgul et al. "Alternative Local Melting-Solidification of Suspended Nanoparticles for Heterostructure Formation Enabled by Pulsed Laser Irradiation." *Advanced Functional Materials* 33, no. 43 (2023): 2304359.

[17] Burhan Ates, Suleyman Koytepe, Ahmet Ulu, Canbolat Gurses, and Vijay Kumar Thakur. "Chemistry, structures, and advanced applications of nanocomposites from biorenewable resources." *Chemical Reviews* 120, no. 17 (2020): 9304-9362.

[18] Vagner de Oliveira Machado, Ângela Leão Andrade, José Domingos Fabris, Erico Tadeu Fraga Freitas, José Maria da Fonte Ferreira, Alice Simon, Rosana Zacarias Domingues et al. "Preparation of hybrid nanocomposite particles for medical practices." *Colloids and Surfaces A: Physicochemical and Engineering Aspects* 624 (2021): 126706.

[19] Is Fatimah, Ganjar Fadillah, Gani Purwiandono, Imam Sahroni, Dyah Purwaningsih, Handy Riantana, Adnan Nur Avif, and Suresh Sagadevan. "Magnetic-silica nanocomposites and the functionalized forms for environment and medical applications: A review." *Inorganic Chemistry Communications* 137 (2022): 109213.

[20] Xiangwen Liu, Dingsheng Wang, and Yadong Li. "Synthesis and catalytic properties of bimetallic nanomaterials with various architectures." *Nano Today* 7, no. 5 (2012): 448-466.

[21] Xiaomin Li, Fan Zhang, and Dongyuan Zhao. "Lab on upconversion nanoparticles: optical properties and applications engineering via designed nanostructure." *Chemical Society Reviews* 44, no. 6 (2015): 1346-1378.

[22] Fei Liu, Yanglong Hou, and Song Gao. "Exchange-coupled nanocomposites: chemical synthesis, characterization and applications." *Chemical Society Reviews* 43, no. 23 (2014): 8098-8113.

Journal Pre-proof

[23] Pannaree Srinoi, Yi-Ting Chen, Varadee Vittur, Maria D. Marquez, and T. Randall Lee. "Bimetallic nanoparticles: enhanced magnetic and optical properties for emerging biological applications." *Applied Sciences* 8, no. 7 (2018): 1106.

[24] Pantaleo Davide Cozzoli, Teresa Pellegrino, and Liberato Manna. "Synthesis, properties and perspectives of hybrid nanocrystal structures." *Chemical Society Reviews* 35, no. 11 (2006): 1195-1208.

[25] Adriana Zaleska-Medynska, Martyna Marchelek, Magdalena Diak, and Ewelina Grabowska. "Noble metal-based bimetallic nanoparticles: the effect of the structure on the optical, catalytic and photocatalytic properties." *Advances in colloid and interface science* 229 (2016): 80-107.

[26] Ahmed Mohsen Ismail, Gergely F. Samu, Ádám Balog, Edit Csapó, and Csaba Janáky. "Composition-dependent electrocatalytic behavior of Au–Sn bimetallic nanoparticles in carbon dioxide reduction." *ACS Energy Letters* 4, no. 1 (2018): 48-53.

[27] Hao Wang, Huan Hao, and Yongxin Li. "Size-dependent electrochemistry and electrocatalysis at single Au@ Pt bimetallic nanoparticles." *The Journal of Physical Chemistry C* 124, no. 45 (2020): 24740-24746.

[28] Clemens Burda, Xiaobo Chen, Radha Narayanan, and Mostafa A. El-Sayed. "Chemistry and properties of nanocrystals of different shapes." *Chemical reviews* 105, no. 4 (2005): 1025-1102.

[29] Manoj B. Gawande, Anandarup Goswami, François-Xavier Felpin, Tewodros Asefa, Xiaoxi Huang, Rafael Silva, Xiaoxin Zou, Radek Zboril, and Rajender S. Varma. "Cu and Cu-based nanoparticles: synthesis and applications in catalysis." *Chemical reviews* 116, no. 6 (2016): 3722-3811.

[30] Nalwa, Hari Singh. "Encyclopedia of nanoscience and nanotechnology." *American Scientific Publishers, Stevenson Ranch, CA* (2004): Vol. 6, p. 815.

[31] Saima Gul, Sher Bahadar Khan, Inayat Ur Rehman, Murad Ali Khan, and M. I. Khan. "A comprehensive review of magnetic nanomaterials modern day theranostics." *Frontiers in Materials* 6 (2019): 179.

[32] Sheng Peng, Chao Wang, Jin Xie, and Shouheng Sun. "Synthesis and stabilization of monodisperse Fe nanoparticles." *Journal of the American Chemical Society* 128, no. 33 (2006): 10676-10677.

[33] Wei-xian Zhang. "Nanoscale iron particles for environmental remediation: an overview." *Journal of nanoparticle Research* 5 (2003): 323-332.

[34] Dongyang Shi, Xia Zhang, Jianji Wang, and Jing Fan. "Highly reactive and stable nanoscale zero-valent iron prepared within vesicles and its high-performance removal of water pollutants." *Applied Catalysis B: Environmental* 221 (2018): 610-617.

[35] Ramadan Eljamal, Osama Eljamal, Ahmed ME Khalil, Bidyut Baran Saha, and Nobuhiro Matsunaga. "Improvement of the chemical synthesis efficiency of nano-scale zero-valent iron particles." *Journal of environmental chemical engineering* 6, no. 4 (2018): 4727-4735.

[36] Armin Dadras Eslamlou, Aliakbar Ghaderiaram, Erik Schlangen, and Mohammad Fotouhi. "A review on non-destructive evaluation of construction materials and structures using magnetic sensors." *Construction and Building Materials* 397 (2023): 132460.

[37] Deepshikha Rathore, Supratim Mitra, Rajnish Kurchania, and R. K. Pandey. "Physicochemical properties of $CuFe_2O_4$ nanoparticles as a gas sensor." *Journal of Materials Science: Materials in Electronics* 29 (2018): 1925-1932.

[38] Run Zhang, Cong Qin, Hari Bala, Yan Wang, and Jianliang Cao. "Recent Progress in Spinel Ferrite (MFe_2O_4) Chemiresistive Based Gas Sensors." *Nanomaterials* 13, no. 15 (2023): 2188.

[39] Yuanyuan Tang, Kaimin Shih, Chengshuai Liu, and Changzhong Liao. "Cubic and tetragonal ferrite crystal structures for copper ion immobilization in an iron-rich ceramic matrix." *RSC advances* 6, no. 34 (2016): 28579-28585.

[40] Deepa Thapa, Nilesh Kulkarni, S. N. Mishra, P. L. Paulose, and Pushan Ayyub. "Enhanced magnetization in cubic ferrimagnetic $CuFe_2O_4$ nanoparticles synthesized from a citrate precursor: the role of Fe^{2+}." *Journal of Physics D: Applied Physics* 43, no. 19 (2010): 195004.

[41] Shameran Jamal Salih, and Wali M. Mahmood. "Review on magnetic spinel ferrite (MFe_2O_4) nanoparticles: From synthesis to application." *Heliyon* 9, no. 6 (2023).

[42] Muhammad Faheem, Xinbai Jiang, Lianjun Wang, and Jinyou Shen. "Synthesis of Cu_2O-$CuFe_2O_4$ microparticles from Fenton sludge and its application in the Fenton process: the key role of Cu_2O in the catalytic degradation of phenol." *Rsc Advances* 8, no. 11 (2018): 5740-5748.

[43] T. Giannakopoulou, L. Kompotiatis, A. Kontogeorgakos, and G. Kordas. "Microwave behavior of ferrites prepared via sol-gel method." *Journal of Magnetism and Magnetic Materials* 246, no. 3 (2002): 360-365.

[44] M. M. Rashad, and O. A. Fouad. "Synthesis and characterization of nano-sized nickel ferrites from fly ash for catalytic oxidation of CO." *Materials Chemistry and Physics* 94, no. 2-3 (2005): 365-370.

[45] E. Hasmonay, J. Depeyrot, M. H. Sousa, F. A. Tourinho, J-C. Bacri, R. Perzynski, Yu L. Raikher, and I. Rosenman. "Magnetic and optical properties of ionic ferrofluids based on nickel ferrite nanoparticles." *Journal of Applied Physics* 88, no. 11 (2000): 6628-6635.

[46] N. Rezlescu, N. Iftimie, E. Rezlescu, C. Doroftei, and P. D. Popa. "Semiconducting gas sensor for acetone based on the fine grained nickel ferrite." *Sensors and Actuators B: Chemical* 114, no. 1 (2006): 427-432.

[47] Yanbin Wang, Hongying Zhao, and Guohua Zhao. "Iron-copper bimetallic nanoparticles embedded within ordered mesoporous carbon as effective and stable heterogeneous Fenton catalyst for the degradation of organic contaminants." *Applied Catalysis B: Environmental* 164 (2015): 396-406.

[48] Yaobin Ding, Lihua Zhu, Nan Wang, and Heqing Tang. "Sulfate radicals induced degradation of tetrabromobisphenol A with nanoscaled magnetic $CuFe_2O_4$ as a heterogeneous catalyst of peroxymonosulfate." *Applied Catalysis B: Environmental* 129 (2013): 153-162.

[49] Kwang Min Yang, Young Jun Hong, and Yun Chan Kang. "Electrochemical Properties of Yolk–Shell-Structured CuO–Fe_2O_3 Powders with Various Cu/Fe Molar Ratios Prepared by One-Pot Spray Pyrolysis." *ChemSusChem* 6, no. 12 (2013): 2299-2303.

Journal Pre-proof

[50] Huimin Wang, Qiulin Zhang, Tengxiang Zhang, Jifeng Wang, Guangcheng Wei, Mo Liu, and Ping Ning. "Structural tuning and NH_3-SCO performance optimization of CuO-Fe_2O_3 catalysts by impact of thermal treatment." *Applied Surface Science* 485 (2019): 81-91.

[51] Yonghui Zhang, Tao He, Shaoxuan Ding, Huawei Li, Wanchao Song, Jincheng Ding, and Jie Lu. "Photo-fenton degradation of RhB via transition metal oxides composite catalyst Fe_3O_4/CuO under visible light optimized using response surface methodology." *Materials Technology* 37, no. 12 (2022): 2347-2359.

[52] Dandan Zhu, Yu Huang, Rong Li, Shiqi Peng, Pengge Wang, and Jun-ji Cao. "Constructing Active Cu^{2+}–O–Fe^{3+} Sites at the CuO–Fe_3O_4 Interface to Promote Activation of Surface Lattice Oxygen." *Environmental Science & Technology* 57, no. 45 (2023): 17598-17609.

[53] Bruce Ravel, and M. A. T. H. E. N. A. Newville. "ATHENA, ARTEMIS, HEPHAESTUS: data analysis for X-ray absorption spectroscopy using IFEFFIT." *Journal of synchrotron radiation* 12, no. 4 (2005): 537-541.

[54] Kimberly Chenoweth, Adri CT Van Duin, and William A. Goddard. "ReaxFF reactive force field for molecular dynamics simulations of hydrocarbon oxidation." *The Journal of Physical Chemistry A* 112, no. 5 (2008): 1040-1053.

[55] Muye Feng, Xi Zhuo Jiang, and Kai H. Luo. "A reactive molecular dynamics simulation study of methane oxidation assisted by platinum/graphene-based catalysts." *Proceedings of the Combustion Institute* 37, no. 4 (2019): 5473-5480.

[56] Qian Mao, Adri CT Van Duin, and K. H. Luo. "Formation of incipient soot particles from polycyclic aromatic hydrocarbons: A ReaxFF molecular dynamics study." *Carbon* 121 (2017): 380-388.

[57] Humphrey, William, Andrew Dalke, and Klaus Schulten. "VMD: visual molecular dynamics." *Journal of molecular graphics* 14, no. 1 (1996): 33-38.

[58] Mark C. Biesinger, Leo WM Lau, Andrea R. Gerson, and Roger St C. Smart. "Resolving surface chemical states in XPS analysis of first row transition metals, oxides and hydroxides: Sc, Ti, V, Cu and Zn." *Applied surface science* 257, no. 3 (2010): 887-898.

[59] Yonglong Shen, Meilan Guo, Xiaohong Xia, and Guosheng Shao. "Role of materials chemistry on the electrical/electronic properties of CuO thin films." *Acta Materialia* 85 (2015): 122-131.

[60] Mark C. Biesinger "Advanced analysis of copper X-ray photoelectron spectra." *Surface and Interface Analysis* 49, no. 13 (2017): 1325-1334.

[61] Anna Białas, Kamil Rugała, Cezary Czosnek, Grzegorz Mordarski, and Jacek Gurgul. "Copper aluminum spinels doped with cerium as catalysts for NO removal." *Catalysts* 10, no. 12 (2020): 1388.

[62] Jacques Ghijsen, Liu-Hao Tjeng, Jan van Elp, Henk Eskes, Jos Westerink, George A. Sawatzky, and Marek T. Czyzyk. "Electronic structure of Cu 2 O and CuO." *Physical Review B* 38, no. 16 (1988): 11322.

[63] Yurii V. Larichev, Boris L. Moroz, and Valerii I. Bukhtiyarov. "Electronic state of ruthenium deposited onto oxide supports: An XPS study taking into account the final state effects." *Applied surface science* 258, no. 4 (2011): 1541-1550.

[64] Kalina Grzelak, Maciej Trejda, and Jacek Gurgul. "Impact of cerium oxide on the state and hydrogenation activity of ruthenium species incorporated on mesocellular foam silica." *Materials* 15, no. 14 (2022): 4877.

[65] Ilia Platzman, Reuven Brener, Hossam Haick, and Rina Tannenbaum. "Oxidation of polycrystalline copper thin films at ambient conditions." *The Journal of Physical Chemistry C* 112, no. 4 (2008): 1101-1108.

[66] Pierre Dubot, D. Jousset, V. Pinet, F. Pellerin, and J. P. Langeron. "Simulation of the LMM auger spectra of copper." *Surface and Interface Analysis* 12, no. 2 (1988): 99-104.

[67] Giuliano Moretti, Amedeo Palma, Ernesto Paparazzo, and Mauro Satta. "Auger parameter and Wagner plot studies of small copper clusters." *Surface Science* 646 (2016): 298-305.

[68] F. Severino, J. L. Brito, J. Laine, J. L. G. Fierro, and A. López Agudo. "Nature of copper active sites in the carbon monoxide oxidation on $CuAl_2O_4$and $CuCr_2O_4$ Spinel type catalysts." *Journal of Catalysis* 177, no. 1 (1998): 82-95.

[69] N. S. McIntyre, and D. G. Zetaruk. "X-ray photoelectron spectroscopic studies of iron oxides." *Analytical Chemistry* 49, no. 11 (1977): 1521-1529.

[70] L. Martinez, D. Leinen, F. Martin, M. Gabas, J. R. Ramos-Barrado, E. Quagliata, and E. A. Dalchiele. "Electrochemical growth of diverse iron oxide (Fe3O4, α-FeOOH, and γ-FeOOH) thin films by electrodeposition potential tuning." *Journal of the Electrochemical Society* 154, no. 3 (2007): D126.

[71] Toru Yamashita, and Peter Hayes. "Analysis of XPS spectra of Fe2+ and Fe3+ ions in oxide materials." *Applied surface science* 254, no. 8 (2008): 2441-2449.

[72] P. Ghods, O. Burkan Isgor, J. R. Brown, F. Bensebaa, and D. Kingston. "XPS depth profiling study on the passive oxide film of carbon steel in saturated calcium hydroxide solution and the effect of chloride on the film properties." *Applied Surface Science* 257, no. 10 (2011): 4669-4677.

[73] Hesham Abdel-Samad, and Philip R. Watson. "An XPS study of the adsorption of chromate on goethite (α-FeOOH)." *Applied Surface Science* 108, no. 3 (1997): 371-377.

[74] Shuai Liu, Zhongbin Dong, Dong Xiang, Yong Jiang, Quanbao Tao, and Yan Cao. "Crossing-link of experimental reducibility tests, XPS characterizations and DFT estimates on ferrite oxygen carriers in CLC." *Applied Catalysis B: Environmental* 238 (2018): 647-655.

[75] Matthew M. Montemore, Matthijs A. Van Spronsen, Robert J. Madix, and Cynthia M. Friend. "O2 activation by metal surfaces: implications for bonding and reactivity on heterogeneous catalysts." *Chemical reviews* 118, no. 5 (2017): 2816-2862.

[76] Rulle Reske, Hemma Mistry, Farzad Behafarid, Beatriz Roldan Cuenya, and Peter Strasser. "Particle size effects in the catalytic electroreduction of CO2 on Cu nanoparticles." *Journal of the American Chemical Society* 136, no. 19 (2014): 6978-6986.

[77] Xianqin Wang, Jonathan C. Hanson, Anatoly I. Frenkel, Jaw-Yong Kim, and Jose A. Rodriguez. "Time-resolved studies for the mechanism of reduction of copper oxides with carbon monoxide: complex behavior of lattice oxygen and the formation of suboxides." *The Journal of Physical Chemistry B* 108, no. 36 (2004): 13667-13673.

[78] Jun-Yu Zhang, Chuan Xia, Hao-Fan Wang, and Cheng Tang. "Recent advances in electrocatalytic oxygen reduction for on-site hydrogen peroxide synthesis in acidic media." *Journal of Energy Chemistry* 67 (2022): 432-450.

[79] Hongcheng Peng, Jun Ren, Yuchao Wang, Yu Xiong, Qichen Wang, Qian Li, Xin Zhao et al. "One-stone, two birds: Alloying effect and surface defects induced by Pt on Cu2− xSe nanowires to boost CC bond cleavage for electrocatalytic ethanol oxidation." *Nano Energy* 88 (2021): 106307.

[80] Claudio Bianchini, and Pierluigi Barbaro, eds. *Catalysis for sustainable energy production*. Wiley-Vch, 2009.

[81] Liang An, T. S. Zhao, and Y. S. Li. "Carbon-neutral sustainable energy technology: Direct ethanol fuel cells." *Renewable and Sustainable Energy Reviews* 50 (2015): 1462-1468.

[82] Sara Pérez-Rodríguez, E. Pastor, and M. J. Lázaro. "Electrochemical behavior of the carbon black Vulcan XC-72R: Influence of the surface chemistry." *International Journal of Hydrogen Energy* 43, no. 16 (2018): 7911-7922.

[83] Xiangnan Chen, Xiaohui Wang, and De Fang. "A review on C1s XPS-spectra for some kinds of carbon materials." *Fullerenes, Nanotubes and Carbon Nanostructures* 28, no. 12 (2020): 1048-1058.

[84] Gabriel P. López, David G. Castner, and Buddy D. Ratner. "XPS O 1s binding energies for polymers containing hydroxyl, ether, ketone and ester groups." *Surface and interface analysis* 17, no. 5 (1991): 267-272.

[85] Guangxing Yang, Lida M. Namin, N. Aaron Deskins, and Xiaowei Teng. "Influence of *OH adsorbates on the potentiodynamics of the CO_2 generation during the electro-oxidation of ethanol." *Journal of Catalysis* 353 (2017): 335-348.

[86] Magdalena Parlinska-Wojtan, Elżbieta Drzymała, Grzegorz Gruzeł, Joanna Depciuch, Mikołaj Donten, and Andrzej Kowal. "Ternary Pt/Re/SnO_2 nanoparticles for ethanol oxidation reaction: Understanding the correlation between the synthesis route and the obtained material." *Applied Catalysis A: General* 570 (2019): 319-328.

[87] Elżbieta Drzymała, Grzegorz Gruzeł, Joanna Depciuch, Miroslawa Pawlyta, Mikołaj Donten, and Magdalena Parlinska-Wojtan. "Ternary Pt/Re/SnO_2/C catalyst for EOR: Electrocatalytic activity and durability enhancement." *Nano Research* 13 (2020): 832-842.

[88] Sebastian D. Pike, Edward R. White, Anna Regoutz, Nicholas Sammy, David J. Payne, Charlotte K. Williams, and Milo SP Shaffer. "Reversible redox cycling of well-defined, ultra-small Cu/Cu_2O nanoparticles." *ACS nano* 11, no. 3 (2017): 2714-2723.

[89] Matija Gatalo, Primož Jovanovič, Urša Petek, Martin Šala, Vid Simon Šelih, Francisco Ruiz-Zepeda, Marjan Bele, Nejc Hodnik, and Miran Gaberšček. "Comparison of Pt–Cu/C with benchmark

Pt–Co/C: metal dissolution and their surface interactions." *ACS Applied Energy Materials* 2, no. 5 (2019): 3131-3141.

[90] O. N. Vrublevskaya, A. B. Shcherbakova, A. A. Kudaka, M. G. Galuza, G. Sevjidsuren, and B. Bolormaa. "Catalytic activity of nickel–copper powder alloys in the processes of electrochemical hydrogen evolution in alkaline solution and ethanol alkaline solution." *Proceedings of the National Academy of Sciences of Belarus, Chemical Series* 58, no. 1 (2022): 36-44.

[91] Jingbo Wen, Zixuan Wan, Xiao Hu, Jianlin Huang, and Xiongwu Kang. "Restructuring of copper catalysts by potential cycling and enhanced two-carbon production for electroreduction of carbon dioxide." *Journal of CO_2 Utilization* 56 (2022): 101846.

[92] A. Kowal, M. Li, M. Shao, K. Sasaki, M. B. Vukmirovic, J. H. Zhang, N. S. Marinkovic, P. Liu, A. I. Frenkel, and R. R. Adzic. "Ternary Pt/Rh/SnO_2 electrocatalysts for oxidizing ethanol to CO_2." *Nature materials* 8, no. 4 (2009): 325-330.

Journal Pre-proof

Journal Pre-proof

Table 1. Sample coding

No.	Sample code	Size of Fe_3O_4 (nm)	Solvent	Laser fluence (mJ/cm^2.pulse)	Cu:Fe (molar ratio)	Repetition time (Hz)
1	PLIS1	5	ethanol	200	1:1	10
2	PLIS2	30	ethanol	200	1:1	10
3	PLIS3	30	Ethyl acetate	200	1:1	10
4	PLIS4	5	ethanol	300	1:1	10
5	PLIS5	30	ethanol	300	1:1	10
6	PLIS6	30	Ethyl acetate	300	1:1	10
7	PLIS7	5	ethanol	300	3:1	10
8	PLIS8	5	ethanol	300	1:3	10
9	PLIS9	5	ethanol	225	1:3	10
10	PLIS10	5	ethanol	225	1:3	33

Journal Pre-proof

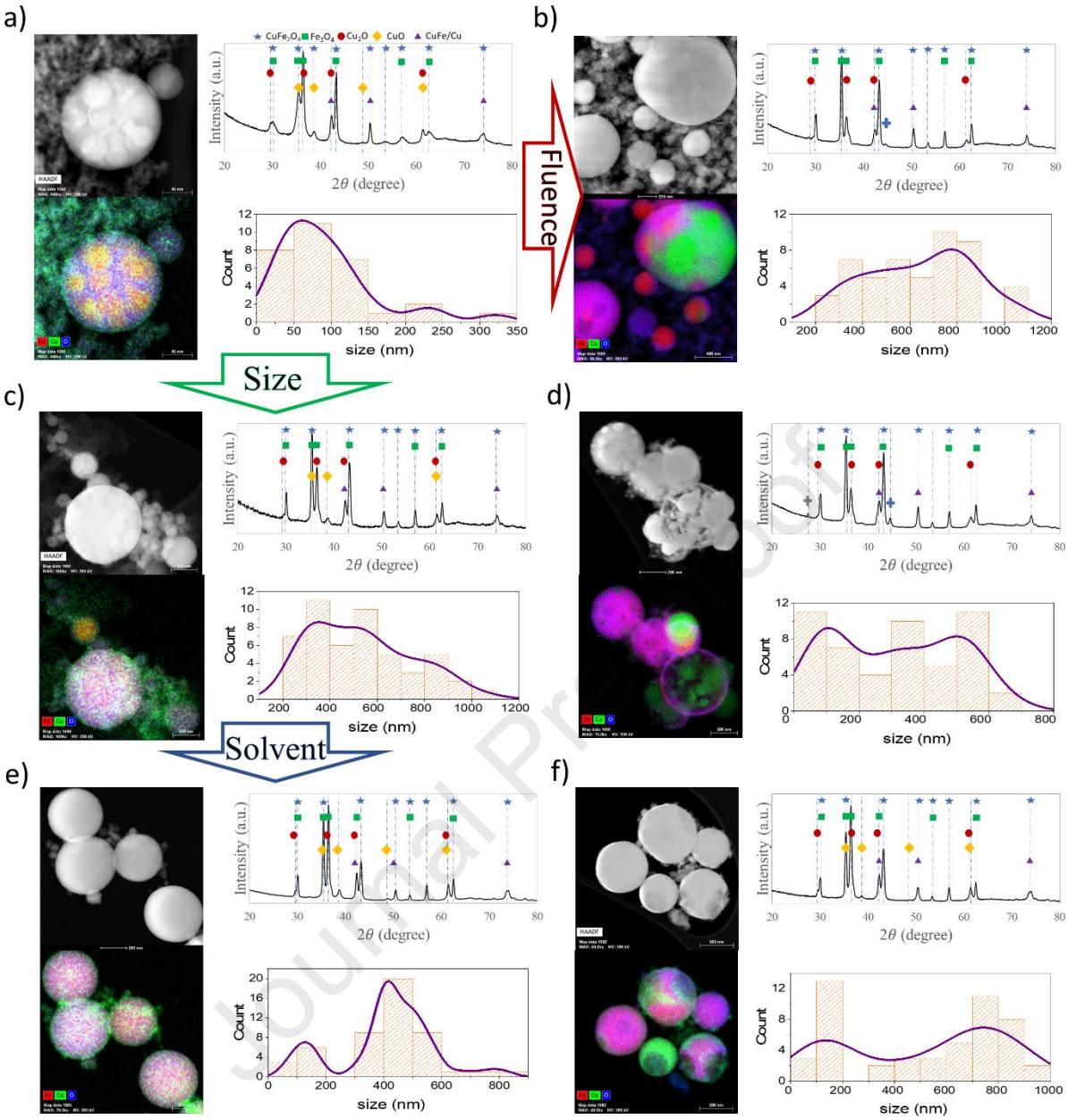
a)
b)
c)
d)
e)
f)
Fluence
Size
Solvent
CuFe2O4 Fe3O4 Cu2O CuO CuFe/Cu
Intensity (a.u.)
2θ (degree)
Count
size (nm)
HAADF

Fig. 1. The microstructural changes observed in samples (a) PLIS1, (b) PLIS4, (c) PLIS2, (d) PLIS5, (e) PLIS3, and (f) PLIS6. HAADF images paired with EDX maps reveal the selective formation of phases in each sample. The EDX maps of PLIS1 and PLIS2 are also represented in Fig. 2a,b for study of the phase formation mechanism. XRD patterns indicate the presence of copper oxides (I and II), copper ferrite, and copper-iron alloy alongside remaining copper and magnetite. The variations in phase presence and intensity validate the influence of synthetic parameters on phase formation during pulsed laser melting. Additionally, SEM-collected (Fig. S3) particle size distribution demonstrates a wide range of sizes containing multimodality, indicating diverse agglomerates with different core particles (Cu and/or Fe_3O_4) leading to multiple size distributions.

Journal Pre-proof

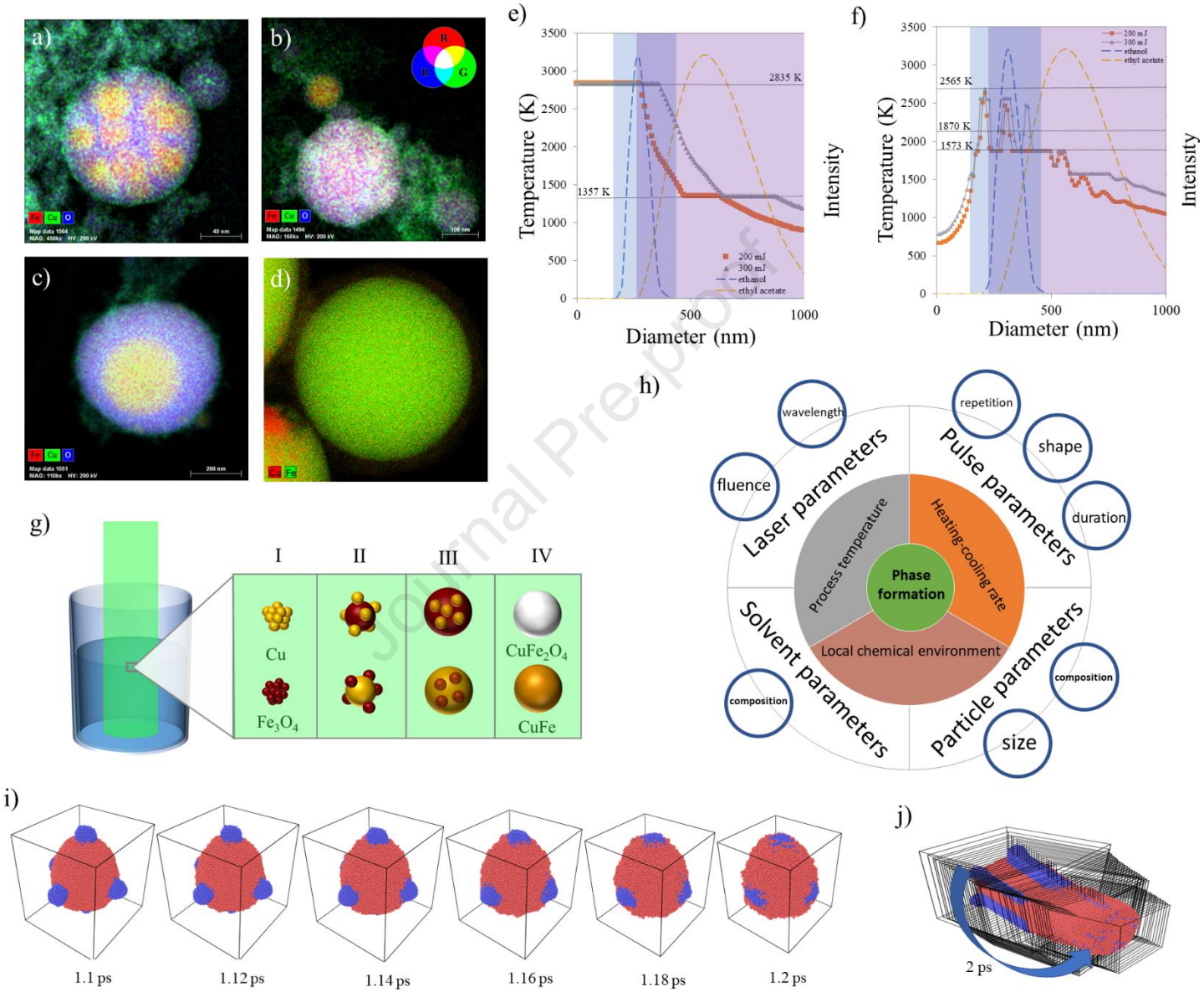

Journal Pre-proof

Journal Pre-proof

Fig. 2. Phase formation mechanism following the pulsed laser melting process. (a) Cu diffusion into the Fe_3O_4 particle resulting in the formation of the CuFe phase in PLIS1, (b) $CuFe_2O_4$ and CuFe formation from Fe_3O_4 in the matrix of copper in PLIS2, (c) Copper ferrite formation in PLIS9, and (d) Observation of CuFe in PLIS10. The EDS maps shown in images (a) through (d) can be found for each sample depicted in Figs. S2 and S4. The size-dependent maximum temperature of (e) Cu and (f) Fe_3O_4 particles irradiated with 200 and 300 mJ/cm^2.pulse fluences. The left and right vertical axes show the temperature of particles and intensity of particle size distribution, respectively. (g) Schematic illustration of the impact of agglomeration on phase formation during the pulsed laser melting process of Cu and magnetite dispersed in liquid. Here four stages are denoted for the mechanism of phase formation in samples containing (I) initial homostructure agglomeration, (II) formation of heterostructure aggregates, (III) diffusion of smaller particles into the bigger core particle, and (IV) phase formation. (h) Schematic illustrating who key factors of phase formation are influenced by synthetic parameters. (i) MD simulation demonstrated the diffusion of iron in ambient temperature into the melted copper particle, as observed also experimentally in Fig. 2a. (j) MD simulation demonstrated the diffusion and distribution of high temperature iron atoms into the melted copper particle. These simulations showed how the lower temperature smaller particle was engulfed by the higher temperature larger particle, resulting in phase formation.

Journal Pre-proof

Journal Pre-proof

Table 2. The BE values (eV) and relative areas of components (%) of Cu 2p 3/2, Cu LMM, O 1s and Fe 2p 3/2 peaks for PLIS samples. Reference (NIST): 711.0 eV - Fe_2O_3, 710.6 eV - Fe_3O_4, 709.5 eV - $Fe_{0.94}O$, 711.2 eV FeOOH. So, we would expect in PLIS7 ($Fe_{0.94}O$ and Fe_2O_3), in PLIS8 (Fe_3O_4 and Fe_2O_3/FeOOH) and in PLIS9 ($Fe_{0.94}O$ and Fe_3O_4). The shift of the Fe 2p line can be caused by the appearance of the core-shell structure, the degree of dispersion and particle size, and the appearance of other oxides, e.g. mixed Cu-Fe spinel ($CuFe_2O_4$).

Core excitation	PLIS1		PLIS2		PLIS3		PLIS4		PLIS5		PLIS6		PLIS7		PLIS8		PLIS9		assignation
	BE (eV)	Area (%)	BE (eV)	Area (%)	BE (eV)	Area (%)	BE (eV)	Area (%)	BE (eV)	Area (%)	BE (eV)	Area (%)	BE (eV)	Area (%)	BE (eV)	Area (%)	BE (eV)	Area (%)	
Cu $2p_{3/2}$	931.4	3.3	931.4	9.5	931.2	8.5	931.0	2.1	930.5	2.0	---		---		930.8	1.7	930.5	2.7	diff. charging
	933.1	73.4	932.6	55.4	932.7	58.9	933.1	72.7	932.7	73.7	932.9	62.8	932.5	39.4	932.8	65.9	932.8	79.8	Cu/Cu_2O
	934.3	19.1	933.6	27.3	933.7	17.7	934.4	15.2	934.2	19.3	934.6	19.2	934.2	29.8	934.1	23.0	934.1	14.0	CuO
	937.4	4.2	935.9	7.8	934.7	14.9	936.1	10.0	936.4	5.0	936.4	18.0	937.0	30.8	936.7	9.4	936.7	3.5	$Cu(OH)_2$
Cu LMM	569.1	27.6	569.3	72.0	569.8	54.0	569.2	26.8	569.2	28.0	569.8	21.0	569.2	35.5	568.2	12.1	568.9	27.3	Cu/CuO
	571.4	72.4	571.1	28.0	571.9	46.0	571.7	73.2	571.7	72.0	572.4	79.0	571.3	64.5	571.2	87.9	571.3	72.7	Cu_2O/$Cu(OH)_2$
O 1s	530.2	53.8	529.4	5.8	530.4	21.8	530.2	14.9	529.9	6.2	---		529.7	5.9	530.0	4.4	529.9	12.5	Me(1)-O*
	531.5	44.1	531.3	20.7	---		531.2	36.9	531.0	8.1	530.8	5.3	530.8	11.2	531.5	18.3	531.6	27.7	Me(2)-O**
	---		532.7	67.3	532.7	73.8	532.7	43.9	532.3	80.2	532.5	79.3	532.5	55.1	532.8	68.8	532.9	52.6	OH^-
	534.0	1.3	534.7	3.7	535.3	4.4	535.1	4.3	534.3	3.8	534.1	9.8	534.6	15.5	534.5	7.7	535.4	7.2	ad. H_2O
	535.8	0.8	536.6	2.5	---		---		536.2	1.7	535.9	5.6	536.2	12.3	536.7	0.8	---		C-O
Fe $2p_{3/2}$	710.1	51.5	709.1	43.9	709.2	26.7	710.4	47.0	710.2	47.2	---		709.9	43.1	710.3	49.2	709.5	36.7	Fe^{2+}
	711.4	48.5	710.6	56.1	710.7	73.3	711.7	53.0	711.8	52.8	---		711.7	56.9	712.0	50.8	710.6	63.3	Fe^{3+}

*Me(1)-O, e.g. CuO, Fe_2O_3
**Me(2)-O, e.g. Cu_2O, FeOOH

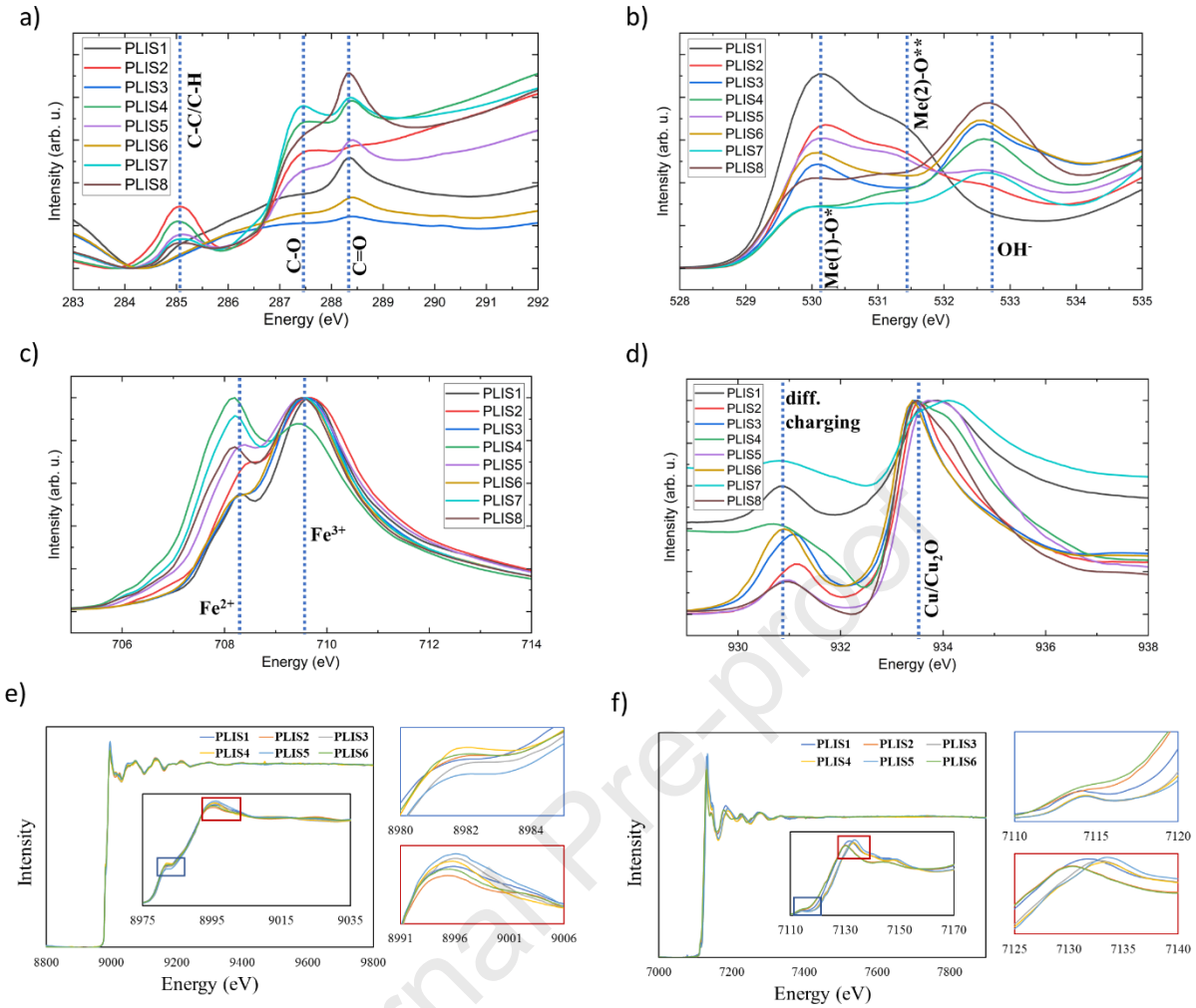

Journal Pre-proof

Fig. 3. Oxidation state analysis of PLIS samples. The analysis of total fluorescence yield (TFY) for the (a) C K-edge, (b) O K-edge, (c) Fe L-edge, and (d) Cu L-edge. TFY signals are able to provide information from deeper layers of the sample compared to other analysis techniques such as TEY and XPS. Interestingly, no detectable signals from hydrogen and water were found in this study, unlike in XPS (Fig. S11) and TEY (Fig. S13) results. The EXAFS and XANES spectra of (e) Cu and (f) Fe K-edges, showing changes in pre-edge and main peak. The quantitative analysis of edge shift in various samples can be found in the Table S6 and S7.

Journal Pre-proof

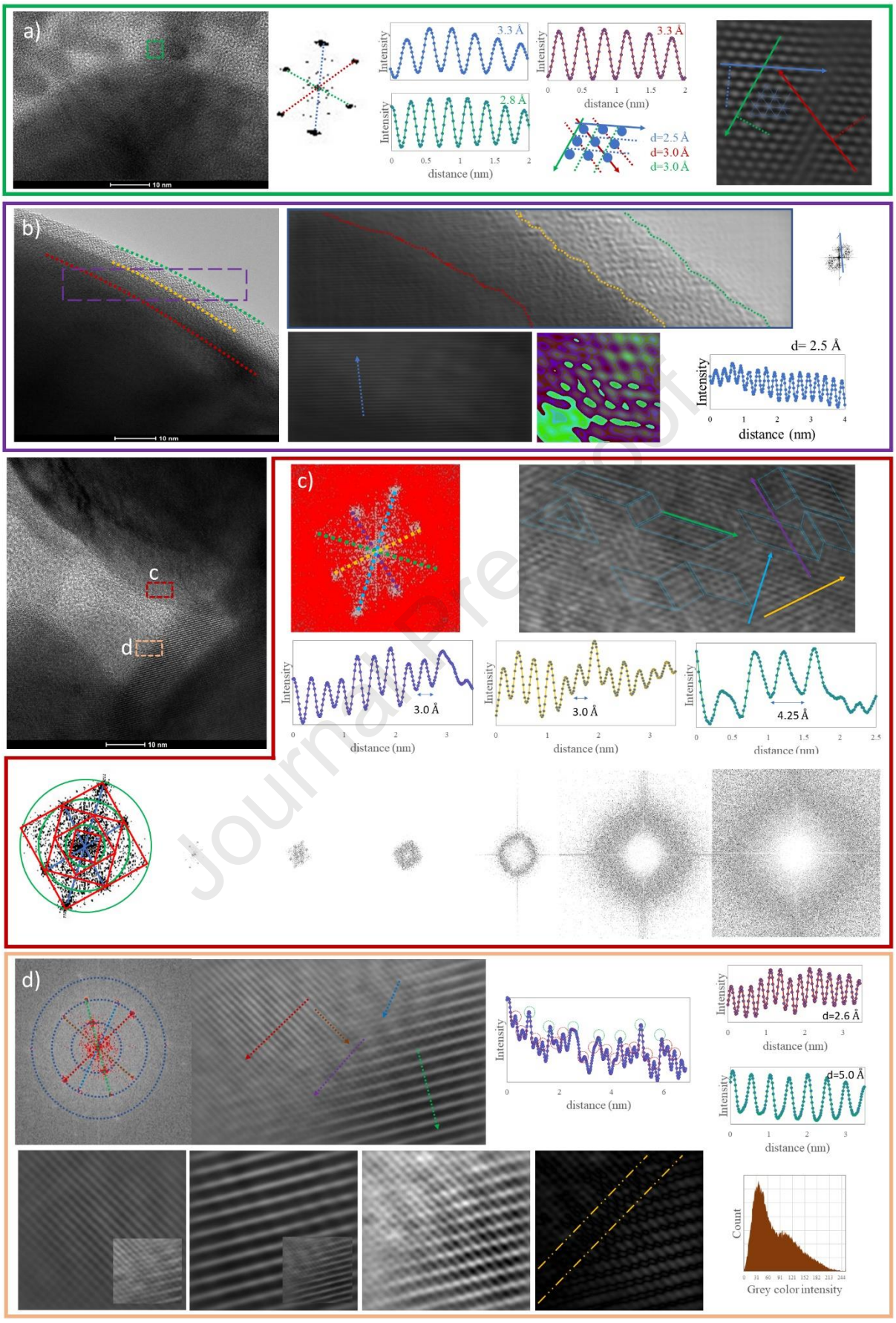

Journal Pre-proof

Journal Pre-proof

Fig. 4. HRTEM analysis of the surface and interface of particles synthesized via the Pulsed Laser Melting method, focusing on CuFe and $CuFe_2O_4$ phases and their corresponding interfaces. (a) A tetragonal-like quantum dot exhibiting d-spacing consistent with the (220) and (311) planes of the $CuFe_2O_4$ phase. Quantum dots on the larger particles may contribute to the phase formation mechanism as illustrated by MD simulations in Fig. 1h. (b) Existence of two non-crystallized layers on a particle surface including a defect-containing crystalline layer and an amorphous layer. The amorphous layer likely formed due to insufficient time (high solidification rate), possibly resulting from viscosity fluctuations at the surface induced by a high concentration of carbon and/or oxygen in the solvent [16]. (c) Evidence of (311) and (220) planes in the cubic CuFe phase. A distinct twin-like structure is visible in certain regions of the particle's surface, marked by subtle variations in the crystal lattice arrangement. (d) The interface between two $CuFe_2O_4$ particles, showing a high degree of alignment between the orientation and spacing of the initial layer of one particle and the adjacent layer of another. This alignment reduces interfacial discrepancy, allowing the particles to achieve minimal interfacial energy.

Journal Pre-proof

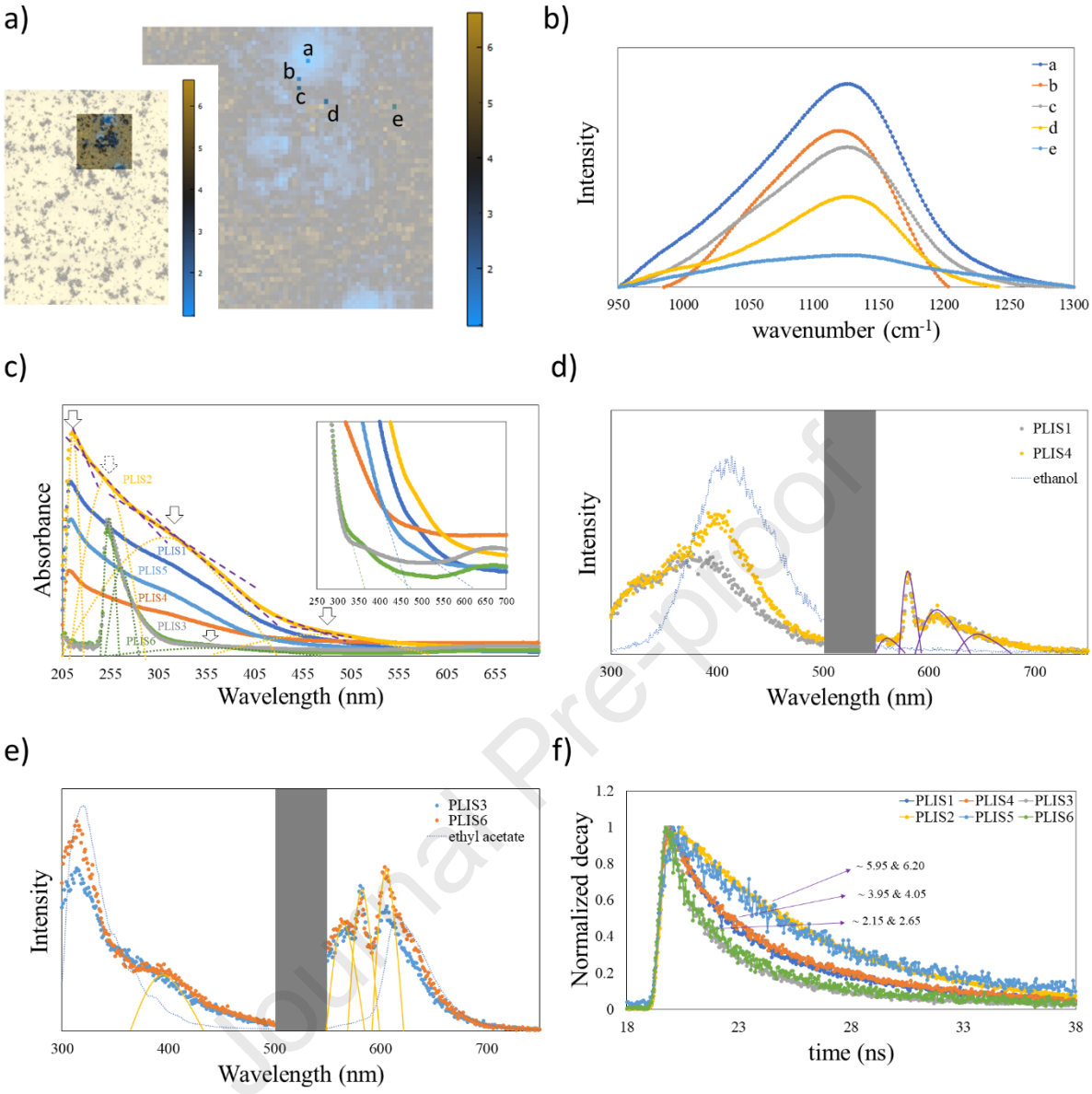

Journal Pre-proof

Journal Pre-proof

Fig. 5. The surface organic contamination and optical properties of PLIS samples. (a) an IR image of the PLIS5 and (b) the ATIR spectra of specific points on the image in part (a), highlighting the stretching pattern of the C-O bond commonly found in primary alcohols. (c) The UV-Vis absorption spectra of the PLIS samples with a focus on the absorption edge enlargement as an indication of the band gap ranges of the samples. The band tailing changes are demonstrated through Gaussian fitting of the PLIS2 and PLIS6 samples, revealing the complex structural features of the samples. The PL spectra of colloidal samples irradiated in (d) ethanol and (e) ethyl acetate. The photoluminescent signals have been analyzed using Gaussian distribution deconvolution to enhance the recognition of PL signals. (f) Normalized decay curves of the samples for the calculation of charge carrier lifetime. It is evident that the initial ingredient plays a predominant role in the optical properties of the samples compared to other factors such as laser fluence.

Journal Pre-proof

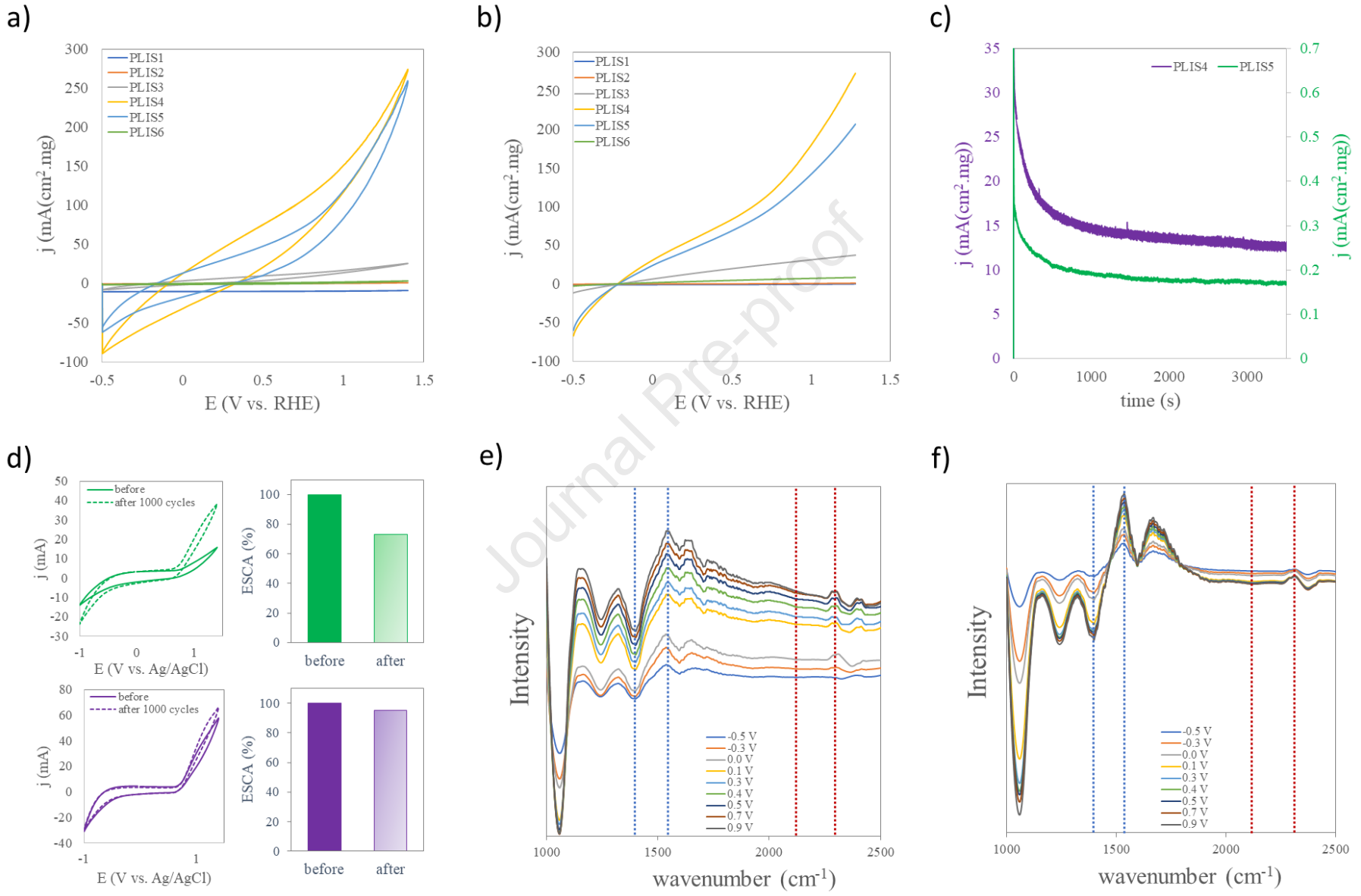

Journal Pre-proof

Fig. 6. Electrocatalysis ethanol oxidation behavior of PLIS samples. (a) Cyclic voltammetry of PLIS/C electrocatalysts in 0.1 M NaOH and sweep rate (50 mV/s). (b) EOR forward scan of the PLIS/C catalysts. (c) Current-time curves recorded at 0.5 vs. Ag/AgCl for 3,600 s in 0.1 M NaOH + 0.5 M ethanol solution. (d) Cyclic voltammogram curves of the PLIS5/C (green) and PLIS4/C (violet) catalysts before and after 10,000 potential cycles accompanied with graphs showing the decrease of ECSA (%). In situ IRRAS spectra recorded during ethanol oxidation on catalysts: (e) PLIS5/C and (f) PLIS4/C, where blue and red dashed line described acetate and carbonate compounds, respectively. IRRAS spectra gives information regarding selectivity of catalyst for carbonate/acetate compounds pathways during EOR. Peaks corresponding to CO_2, CO, CH_3CHO and CH_3COOH were marked. Bands corresponding to acetate compounds such as CH_3COO and HCO^{3-} /CO_3^{2-} are visible around 1550 cm^{-1} and 1415 cm^{-1}, while they are around 2100 cm^{-1} and 2400 $cm^{-1}$for carbonate compounds.

Journal Pre-proof

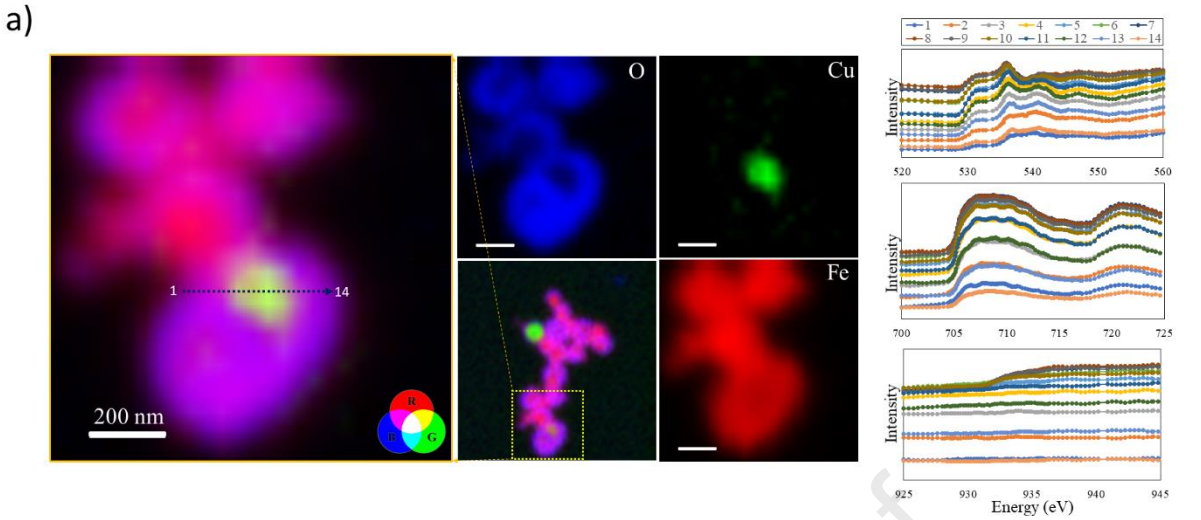

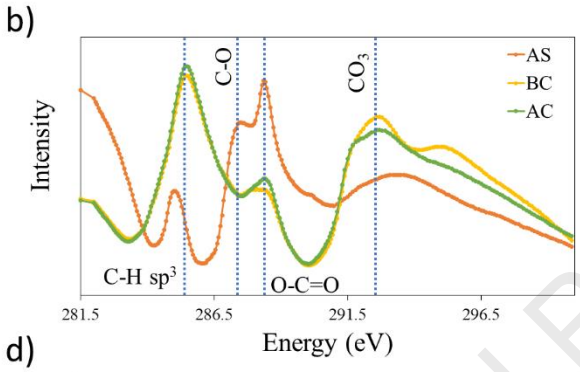

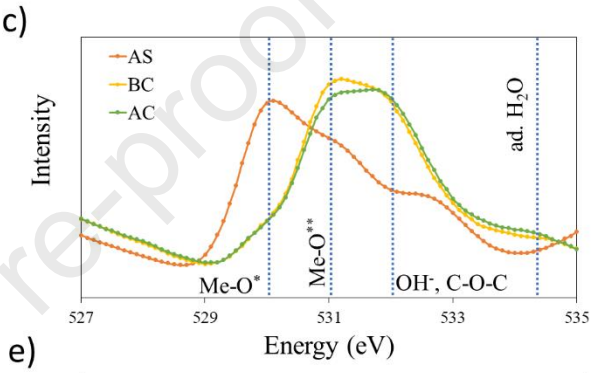

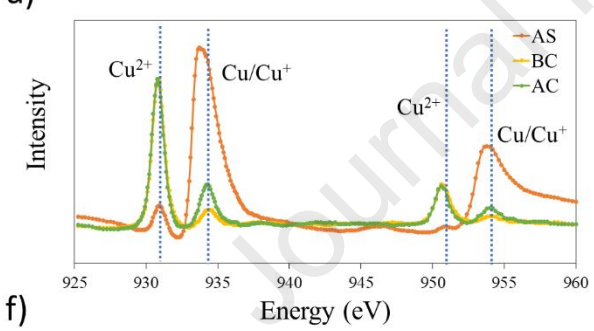

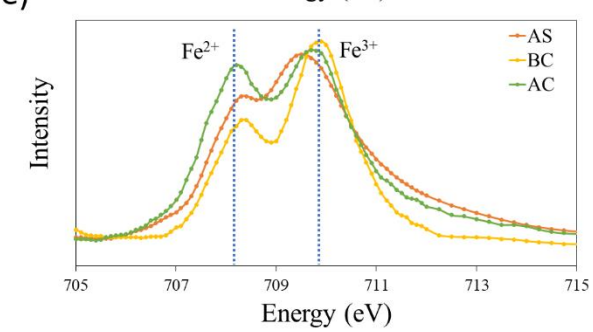

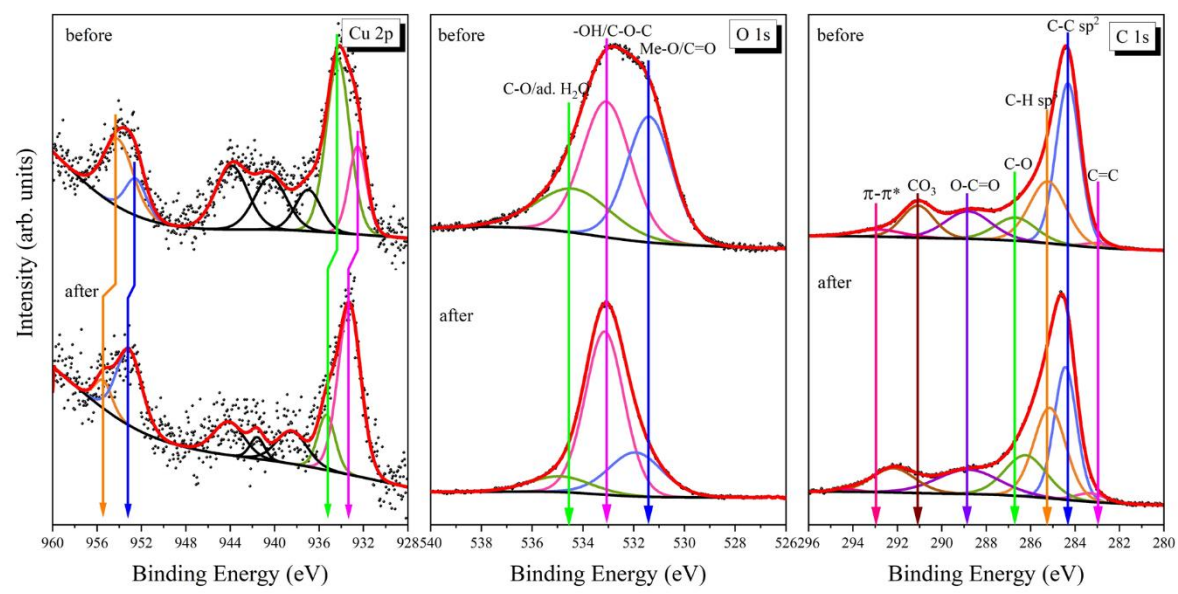

Journal Pre-proof

Journal Pre-proof

Fig. 7. Oxidation state analysis of PLIS sample before and after electrocatalysis. (a) Synchrotron-based STXM examination of a particle cluster located within the carbon bed in PLIS4/C catalyst after catalysis demonstrating a heterostructure resembling CuFe/copper ferrite formed in the matrix of magnetite. The analysis of total fluorescence yield (TFY) for the (b) C K-edge, (c) O K-edge, (d) Cu L-edge, and (e) Fe L-edge. TFY signals are able to provide information from deeper layers of the sample compared to other analysis techniques such as TEY and XPS. (f) XPS analysis of Cu 2p, O 1s and C 1s edges of PLIS sample before and after electrocatalysis. The peaks were deconvoluted carefully for quantitative analysis of chemical phase variations in the sample. The quantitative XPS results have been reported in Table 3.

Journal Pre-proof

Table 3. The BE values (eV) and relative areas of components (%) of Cu $2p_{3/2}$, Cu LMM, O 1s, and C 1s peaks for PLIS4 sample before and after electrocatalysis ethanol oxidation.

Core excitation	before		after		assignation
	BE (eV)	Area (%)	BE (eV)	Area (%)	
Cu $2p_{3/2}$	932.5	27.6	---	---	Cu_xFe_y/Cu/Cu_2O
	---	---	933.3	80.0	CuO
	934.3	72.4	---	---	$CuFe_2O_4$ (O_h)
	---	---	935.3	20.0	$Cu(OH)_2$, $CuFe_2O_4$ (T_d)
Cu LMM	569.4	20.0	570.2	34.0	Cu/CuO
	571.4	80.0	572.1	66.0	Cu_2O/$Cu(OH)_2$
O 1s	531.4	36.6	531.9	24.4	Me-O^*, C=O
	533.1	42.5	533.1	65.6	OH^-, C-O-C
	534.4	20.9	534.9	10.0	ad. H_2O, aromatic C-O
C 1s	282.9	1.3	283.3	2.3	C=C
	284.3	40.9	284.4	28.7	C-C sp^2
	285.2	23.8	285.1	27.9	C-H sp^3
	286.7	9.9	286.2	16.5	C-O
	288.8	13.3	288.8	14.6	O-C=O
	291.1	10.8	292.2	10.0	CO_3

Journal Pre-proof

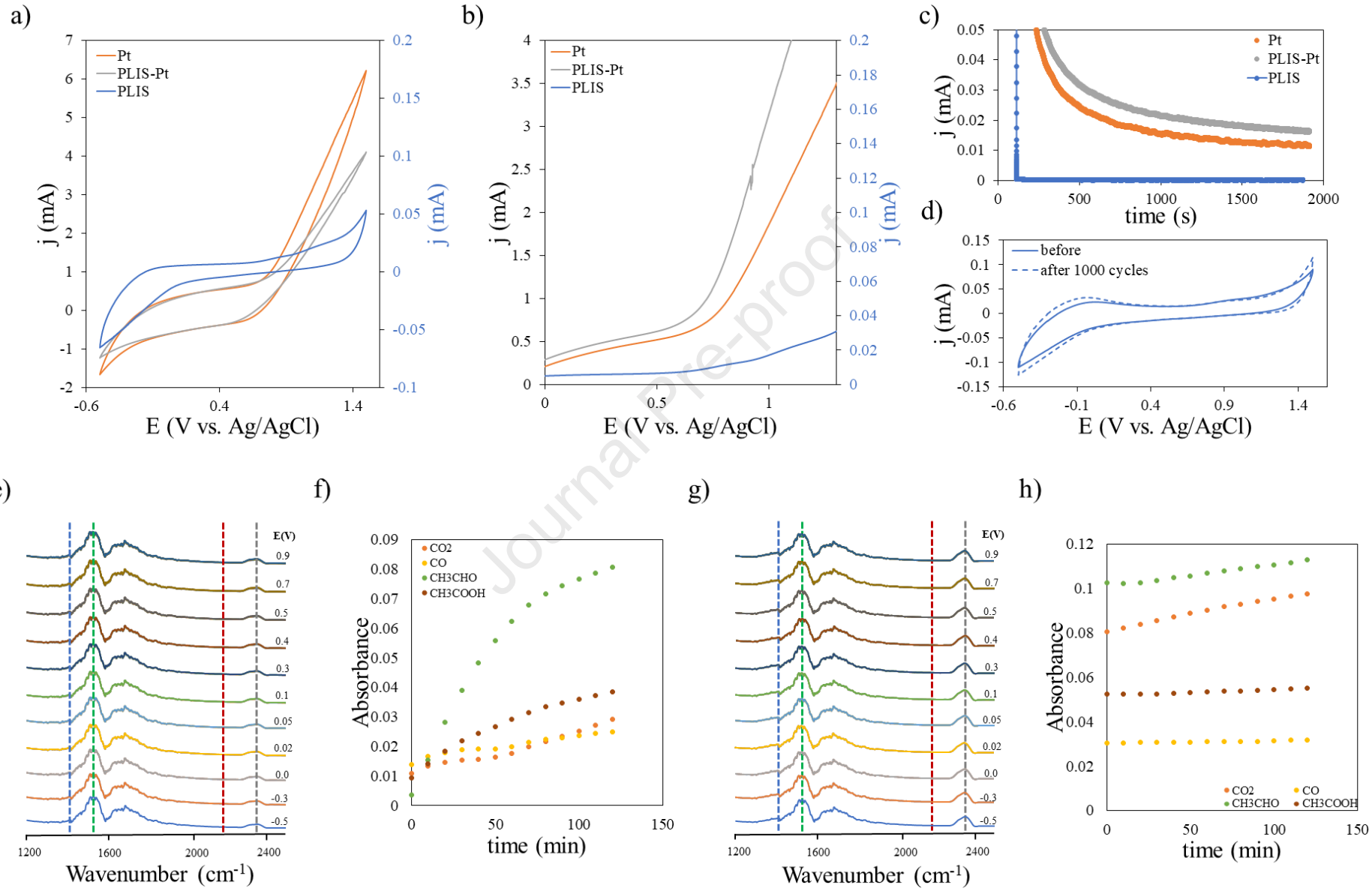

Journal Pre-proof

Fig. 8. The behavior of PLIS sample as the support for electrocatalysis ethanol oxidation in acidic environment. Cyclic voltammetry of (a) PLIS/C, Pt/C and PLIS-Pt/C electrocatalysts and (b) EOR forward scan of the PLIS/C, Pt/C and PLIS-Pt/C catalysts. All curves were recorded in 0.1 M $HClO_4$ + 0.5 M ethanol solution at a scan rate of 50 mV/s at room temperature. (c) Current-time curves recorded at 0.5 vs. Ag/AgCl for 1800 s in 0.1 M $HClO_4$ + 0.5 M ethanol solution for PLIS/C, Pt/C and PLIS-Pt/C, and (d) cyclic voltammogram curves of the PLIS-Pt/C catalyst before and after 10000 potential cycles in 0.1 M $HClO_4$ solution. In situ IRRAS spectra recorded during ethanol oxidation on (e) PLIS/C and (g) PLIS-Pt/C catalysts collected for different potentials in acidic environment. Time-dependent chemical products synthesized during electrocatalysis process and measured using in-situ IRRAS for (f) PLIS/C and (h) PLIS-Pt/C. In spectra peaks originating from CO_2, CO, CH_3CHO and CH_2COOH are marked by grey, red, green and blue, respectively.

Journal Pre-proof

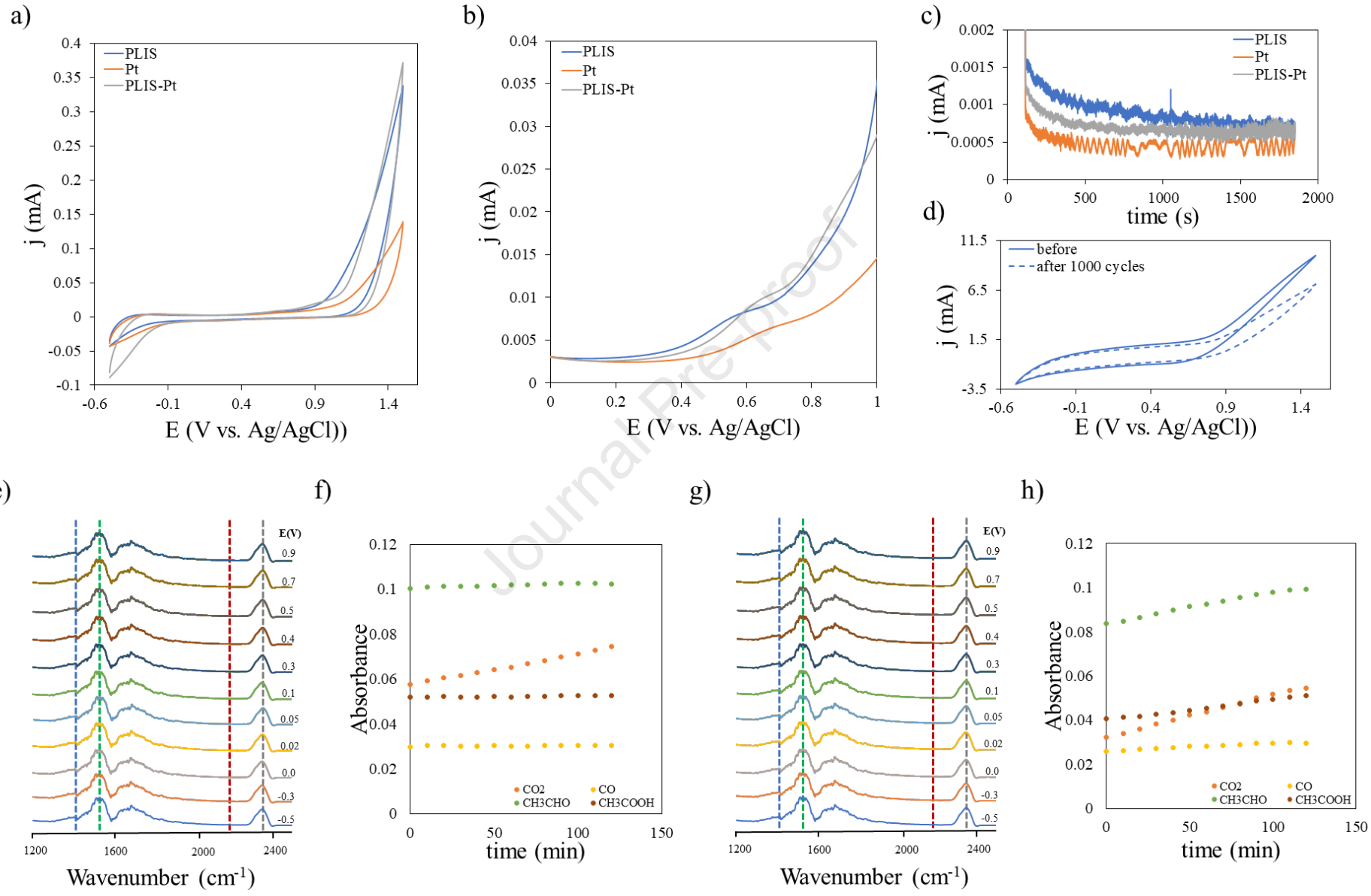

Journal Pre-proof

Fig. 9. Behavior of the PLIS sample as a support for electrocatalytic ethanol oxidation in an alkaline environment. (a) Cyclic voltammetry of PLIS/C, Pt/C, and PLIS-Pt/C electrocatalysts and (b) EOR forward scan of PLIS/C, Pt/C, and PLIS-Pt/C catalysts. All curves were recorded in a 0.1 M NaOH + 0.5 M C_2H_5OH solution at a scan rate of 50 mV/s at room temperature. (c) Current-time curves recorded at 0.5 V vs. Ag/AgCl for 1800 s in 0.1 M NaOH + 0.5 M ethanol solution for PLIS/C, Pt/C, and PLIS-Pt/C, and (d) cyclic voltammogram curves of the PLIS-Pt/C catalyst before and after 1000 potential cycles in 0.1 M NaOH solution. In situ IRRAS spectra recorded during ethanol oxidation on (e) PLIS/C and (g) PLIS-Pt/C catalysts, collected at different potentials in an alkaline environment. Time-dependent chemical products generated during the electrocatalytic process and measured using in-situ IRRAS for (f) PLIS/C and (h) PLIS-Pt/C. In the spectra, peaks originating from CO_2, CO, CH_3CHO, and CH_2COOH are marked in grey, red, green, and blue, respectively.

Journal Pre-proof

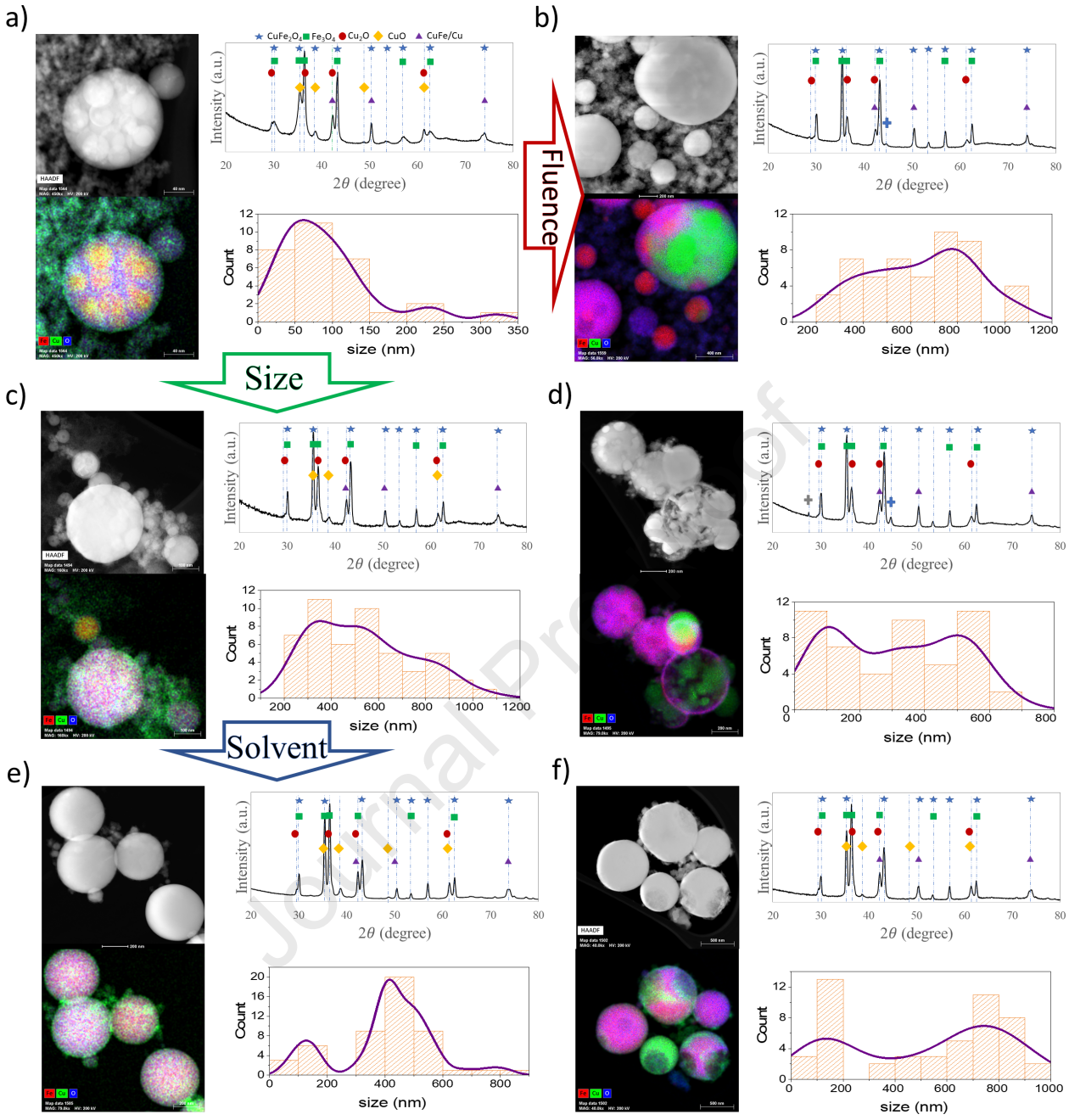

Journal Pre-proof

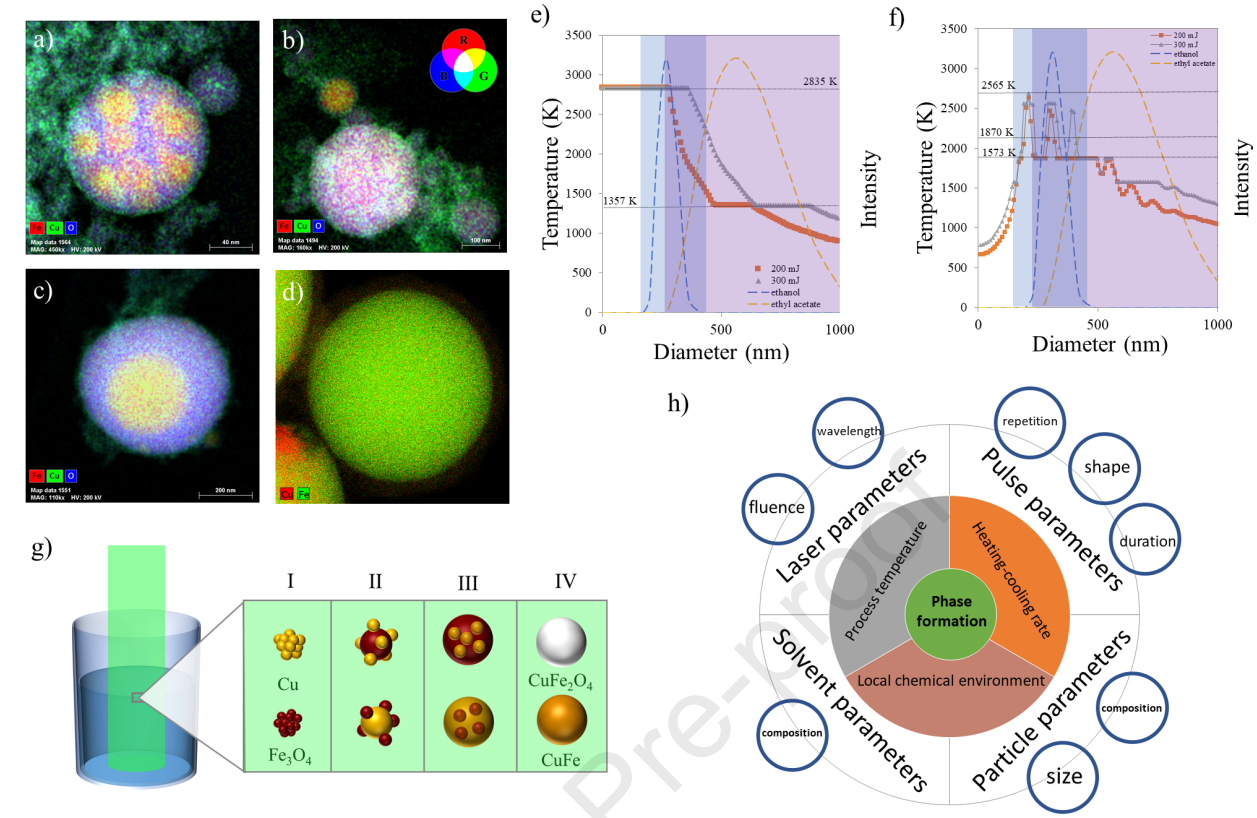

Journal Pre-proof

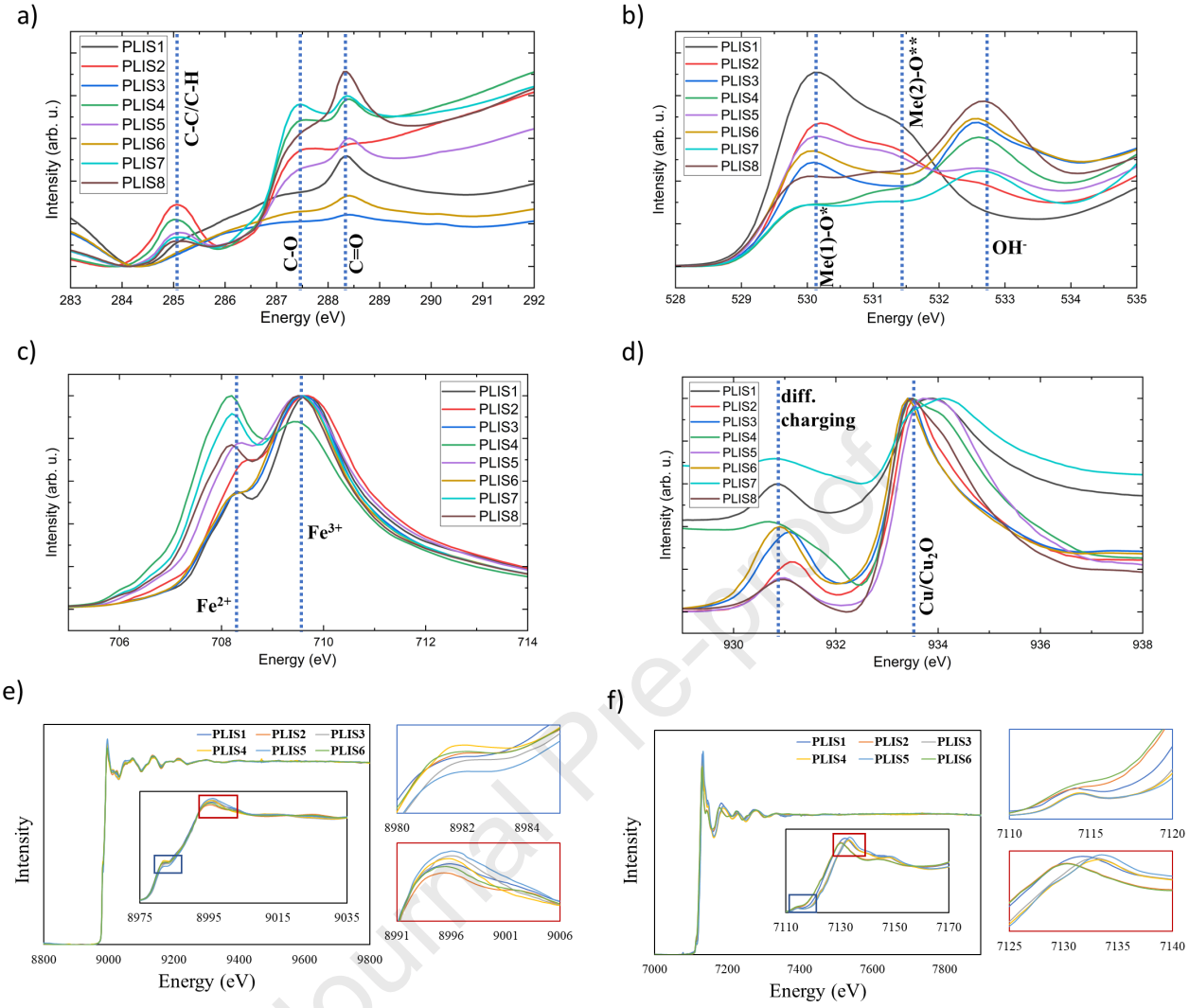

Journal Pre-proof

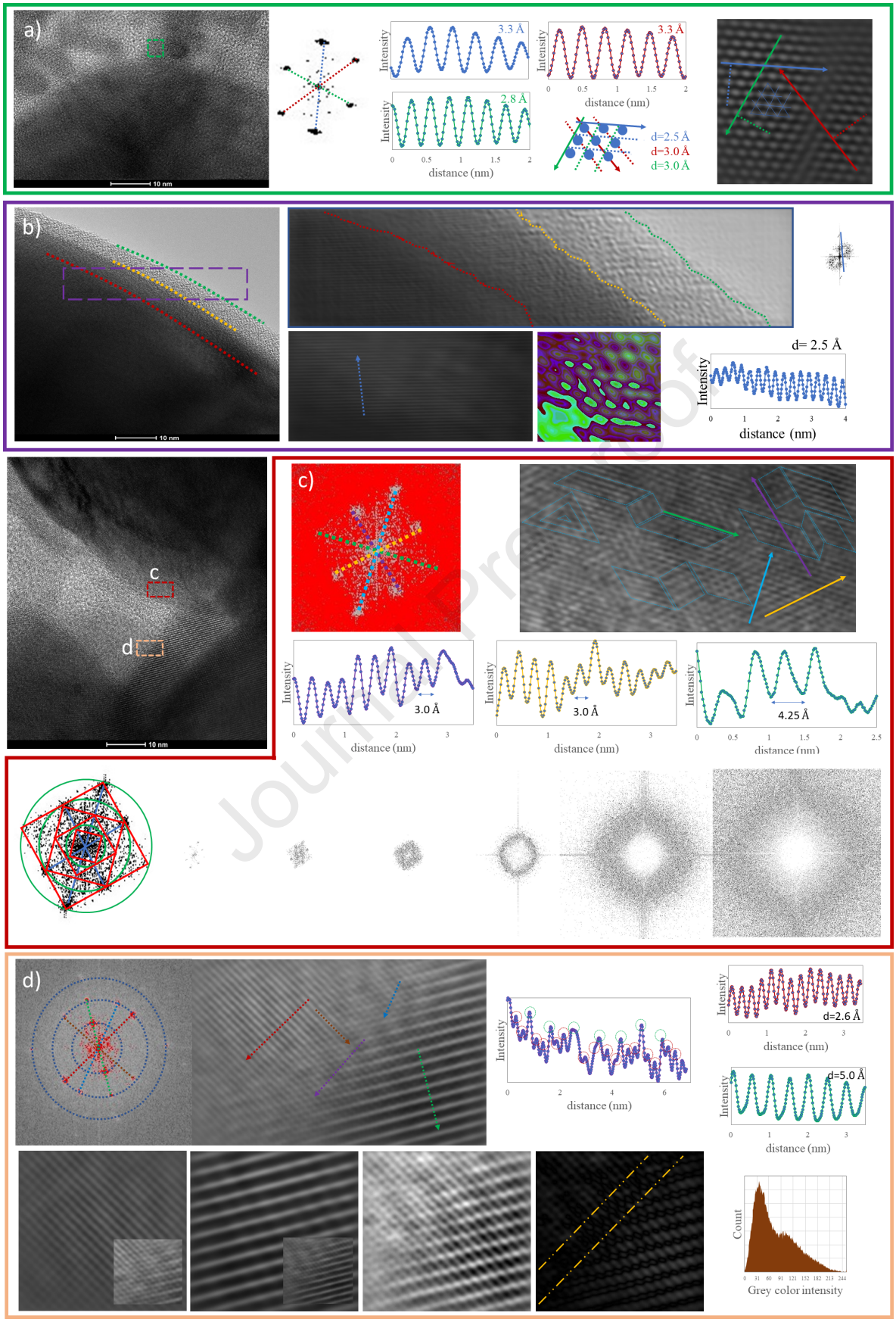

Journal Pre-proof

a)

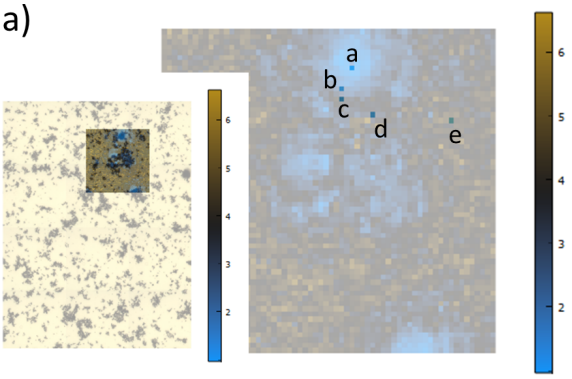

b)

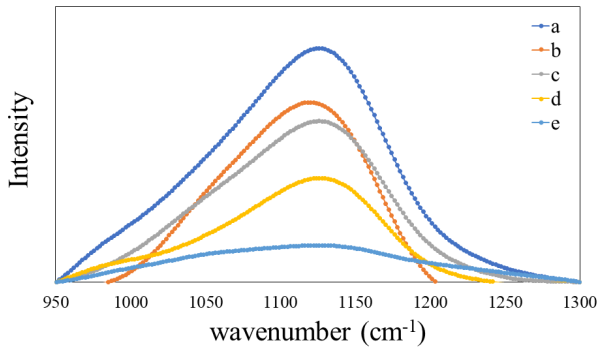

c)

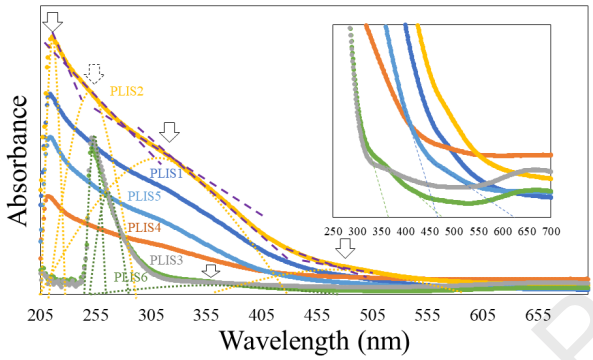

d)

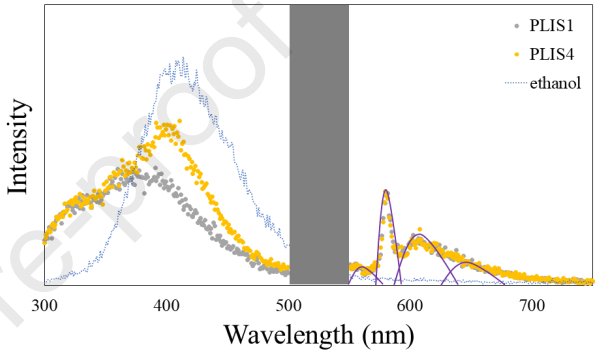

e)

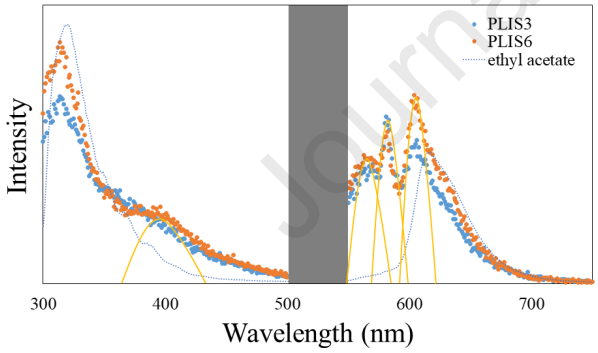

f)

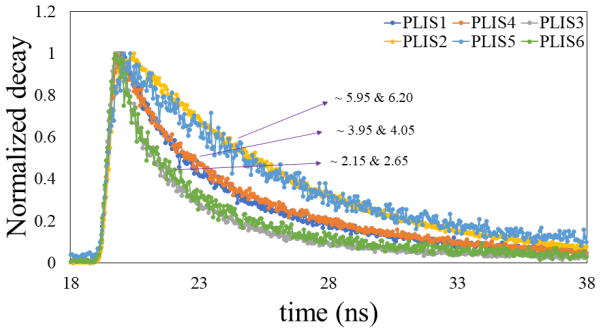

Journal Pre-proof

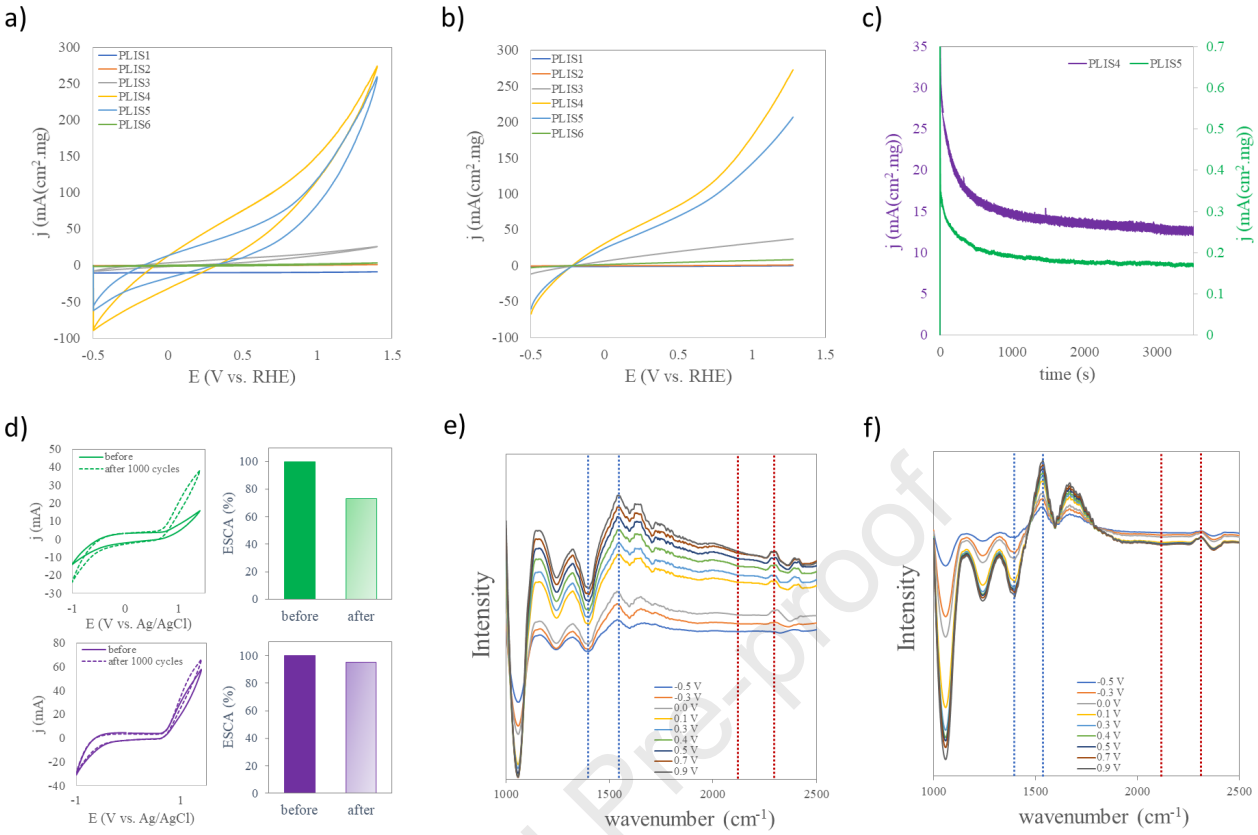

Journal Pre-proof

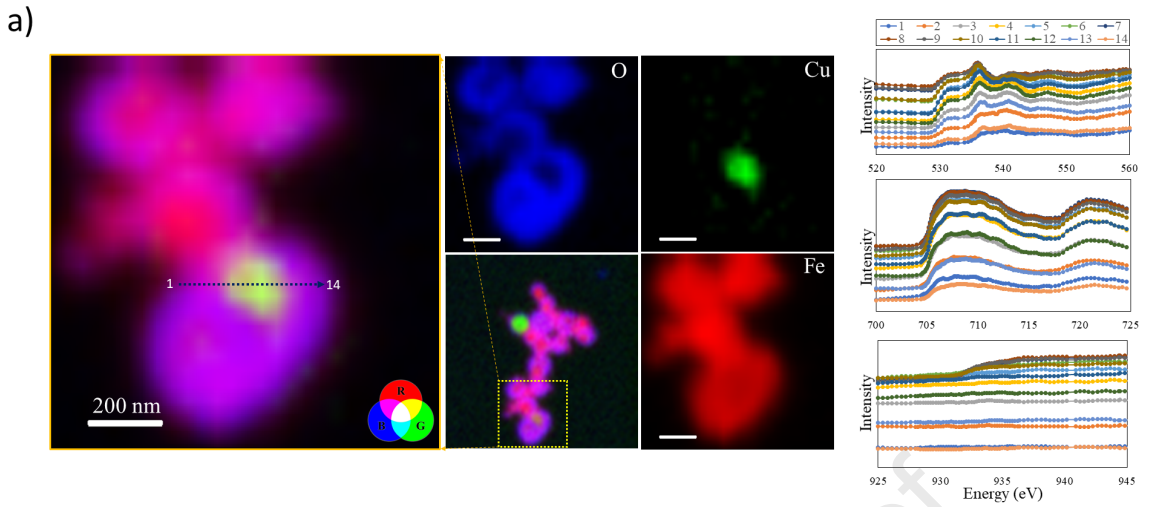

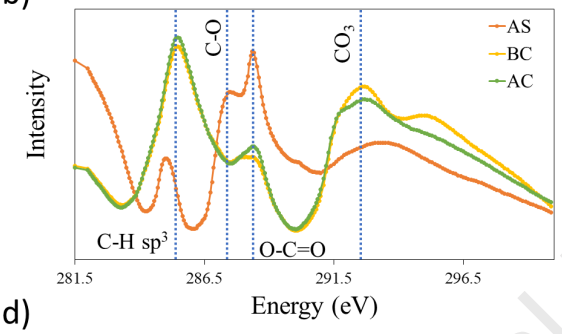

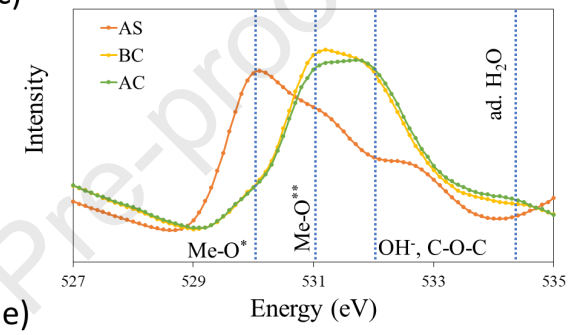

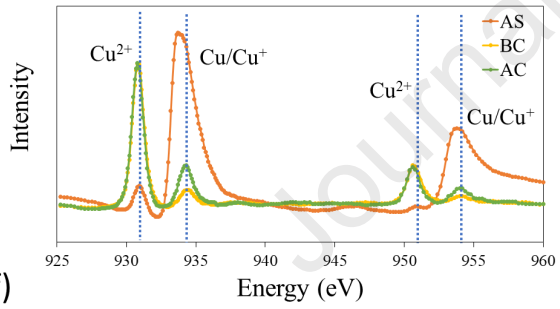

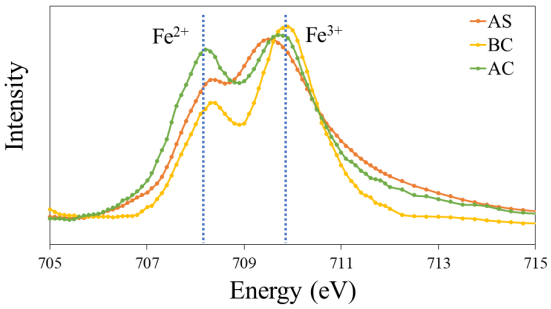

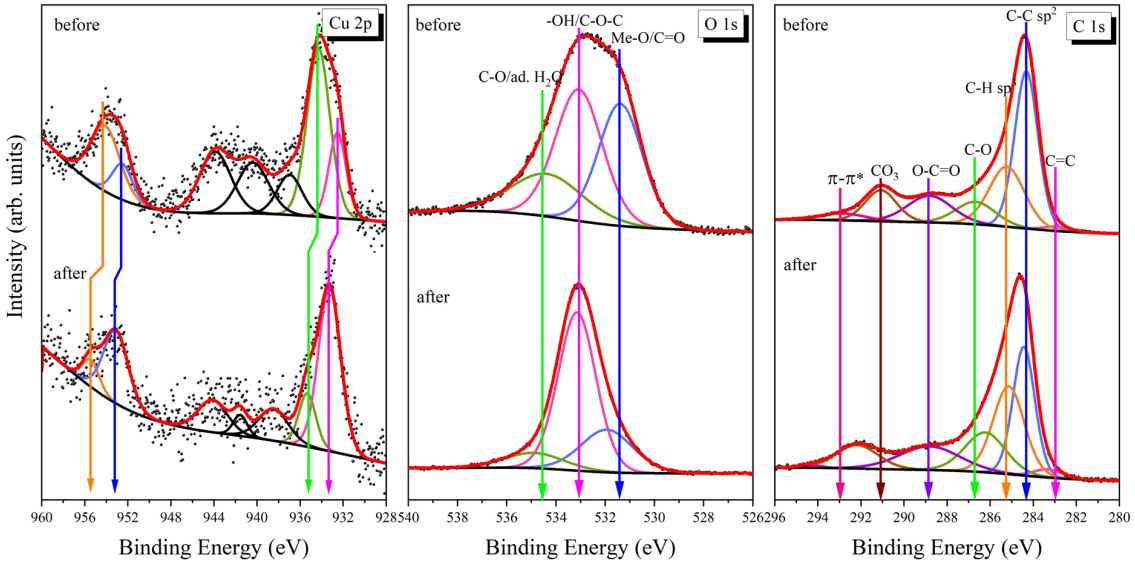

Journal Pre-proof

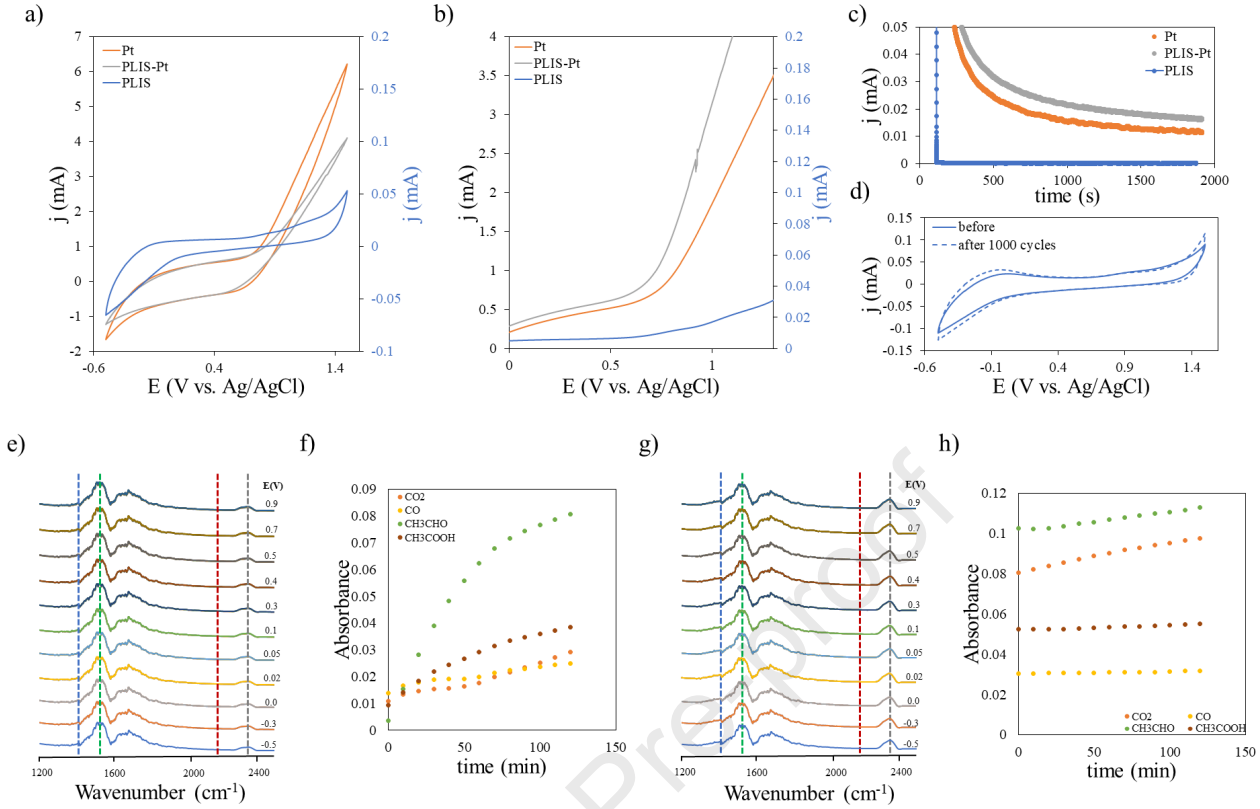

Journal Pre-proof

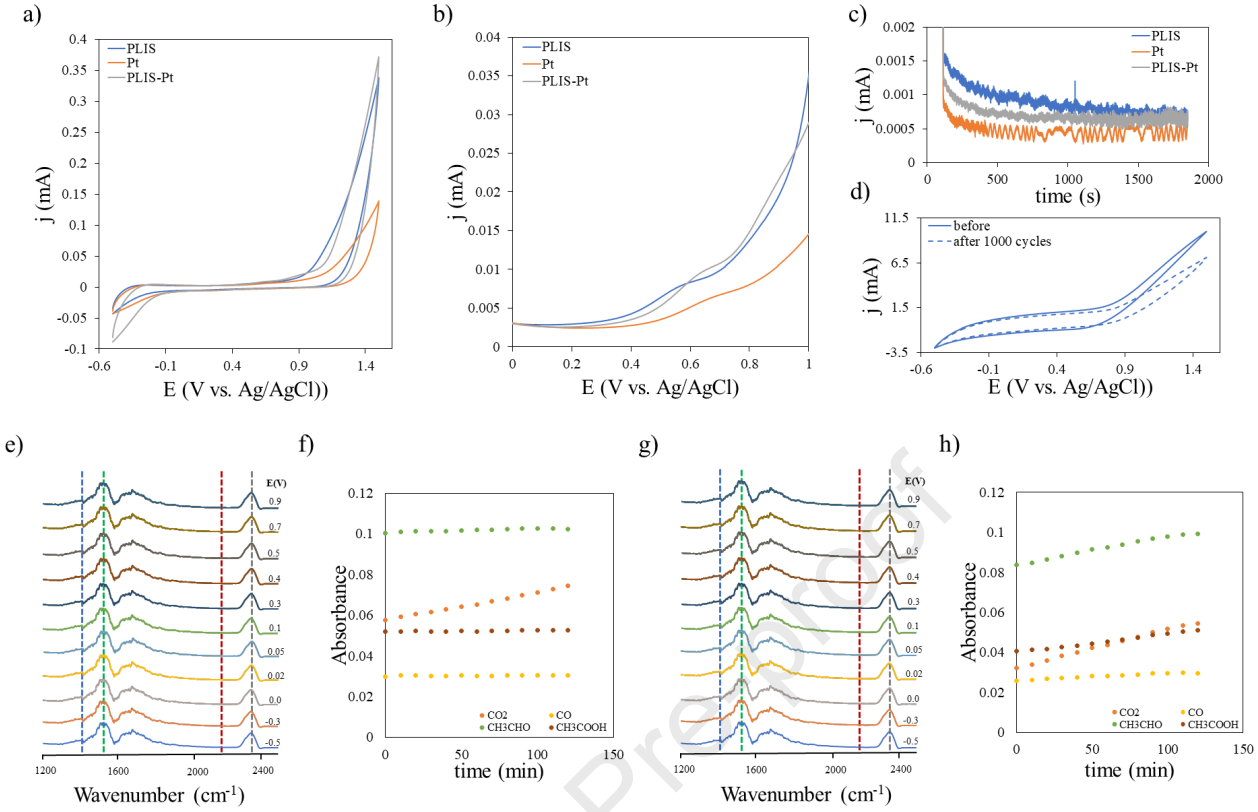

Journal Pre-proof

Journal Pre-proof

Highlights

- Phase formation studied via high-temperature solid-liquid interface analysis.
- Temperature, cooling rate, and local chemistry identified as key phase factors.
- Synthetic parameters classified by impact on key factors for phase formation.
- Composite particles show high catalytic activity as main catalysts and Pt supports.
- Laser-activated surfaces with composite oxidation states yield active structures.

Journal Pre-proof

Journal Pre-proof

Declaration of interests

☐ The authors declare that they have no known competing financial interests or personal relationships that could have appeared to influence the work reported in this paper.

☒ The authors declare the following financial interests/personal relationships which may be considered as potential competing interests:

Mohammad Sadegh Shakeri reports travel was provided by Central European Research Infrastructure Consortium (CERIC-ERIC). Mohammad Sadegh Shakeri reports financial support was provided by Polish National Science Centre. Zaneta Swiatkowska-Warkocka reports financial support was provided by Polish National Science Centre. Other authors declare that they have no known competing financial interests or personal relationships that could have appeared to influence the work reported in this paper.

Journal Pre-proof